Modeling the Effect of Particle Diameter and Density on Dispersion in an Axisymmetric Turbulent Jet

Christopher James Sebesta

Thesis submitted to the Faculty of the

Virginia Polytechnic Institute and State University

In partial fulfillment of the requirements for the degree of

Master of Science

In

Mechanical Engineering

Kenneth Ball, Chair
Brian Lattimer
Robert Masterson

April 25, 2012
Blacksburg, Va

Keywords: Turbulent Jet, Entrainment, Dispersion, CFD, Multiphase Flow

Modeling the Effect of Particle Diameter and Density on Dispersion in an Axisymmetric Turbulent Jet

Christopher James Sebesta

Abstract

Creating effective models predicting particle entrainment behavior within axisymmetric turbulent jets is of significant interest to many areas of study. Research into multiphase flows within turbulent structures has primarily focused on specific geometries for a target application, with little interest in generalized cases. In this research, the entrainment characteristics of various particle sizes and densities were simulated by determining the distribution of particles across a surface after the particles had fallen out of entrainment within the jet core. The model was based on an experimental set-up created by Lieutenant Zachary Robertson, which consists of a particle injection system designed to load particles into a fully developed pipe [1]. This pipe flow then exits into an otherwise quiescent environment (created within a wind tunnel), creating an axisymmetric turbulent round jet. The particles injected were designed to test the effect of both particle size and density on the entrainment characteristics.

The data generated by the model indicated that, for all particle types tested, the distribution across the bottom surface of the wind tunnel followed a standard Gaussian distribution. Experimentation yielded similar results, with the exception that some of the experimental trials showed distributions with significantly non-zero skewness. The model produced results with the highest correlation to experimentation for cases with the smallest Stokes number (small size/density), indicating that the trajectory of particles with the highest level of interaction with the flow were the easiest to predict. This was contrasted by the high Stokes number particles which appear to follow standard rectilinear motion.

Dedication

To my parents, Roxanne and Stephen Sebesta…

for their countless hours of encouragement over the years

Acknowledgement

I would like to thank Lieutenant Zachary Robertson for his time and effort working on the experimental side of this research project, producing results for validation. I would also like to thank Debamoy Sen for his help in trouble shooting my simulations. Finally, I would like to thank Dr. Kenneth Ball for this assistance in working through the multiple iterations of the design for this project.

Table of **Contents**

List of Figures

List of Tables

Chapter 1: Introduction

Effective modeling of particle dispersion is critical to many industrial applications in which controlled conveying of particles is required, including combustion reactors and pneumatic transport processes. An application that has gained significant interest in recent years following the anthrax attacks of 2001 is the modeling of particle dispersion as it relates to chemical, biological, radiological, and nuclear (CBRN) attacks. The ability to predict potential particle dispersion patterns from an initial release of contaminants as well as re-introduction by entrainment would significantly improve the ability to respond to and decontaminate areas affected by such attacks. The primary emphasis of this study is the effect of particle sizes (diameter for spherical cases) and particle density on the entrainment characteristics of heavy particles in an axisymmetric-turbulent jet. Of special interest is modeling the dispersion characteristics of anthrax; this study if a first step toward that application.

While a significant amount of research has been dedicated toward modeling of particle and gaseous dissipation within confined spaces, the cases studied are typically on a very specific geometry or location such as the San Francisco Airport evaluated during the PROACT program leaving a need for experimental and simulation results for generalized cases [2, 3]. This study instead focuses on a simple geometry with applications to multiple cases of CBRN attack distribution including conventional aerosol generators or secondary infection from respiration (including coughing and sneezing).

The ability to decontaminate a building (or even a single office) is a time consuming and often inefficient process. The modern methods of decontamination fall into a "zero-tolerance" policy, where any area or surface must test totally free of contaminants to be classified as clean [4]. In order to improve this process, a better ability to predict particle dispersion based on known characteristics would allow targeted decontamination of affected areas.

The model generated mimics the experimental set up pictured below in Figure 1, where a nozzle with an inlet diameter of 2 inches ejects into a quiescent air environment, producing an axisymmetric jet. Particles were then added via an injection system, modeled as a mono-disperse surface injection across the nozzle. The properties of this injection (particle size and density) were altered ranging from 6mm to 1mm with densities of 2500 kg/m^3 for the glass type used,

3700 kg/m^3 for Zirconia/Silica, 5500 kg/m^3 for the Zirconia, and 7900 kg/m^3 for chrome steel.

Figure 1: Free Jet Controlled Quiescent Environment [1]

The main objectives of this research project include:

1) Develop an effective model for a turbulent axisymmetric jet
2) Evaluate the dispersion properties of spherical particles of varying diameter and density, with special interest in displacement in the direction of the jet flow to determine viable entrainment characteristics
3) Compare the dispersion patterns to ongoing experimental results for validation of statistical properties of dispersion generated by the model

Chapter 2: Background and Literature Review

2.1 Motivation: Bioterrorism Attacks, Health and Containment

Research focused on predicting, preventing, and containing the effects of bioterrorism attacks has been high as a result of the 2001 anthrax letter incidents. While these attacks only resulted in 5 deaths and 17 surviving the infection, interest has been high since that time with a heavy focus on Bacillus Anthracis (the bacteria responsible for anthrax infections, hereafter referred to as anthrax) due to its lethality and psychological effect. Anthrax infections typically come in three varieties: ingestion, cutaneous, and inhalation. Cutaneous infections typically arise from exposure to infected animals through scratches in the skin. It is the most common form of infection in humans, but is only fatal in up to 20% of untreated individuals. Infection via ingestion occurs usually by consuming meat from infected livestock, but is rare in humans and is not typically fatal. The method of infection that is the greatest threat to national security is inhalation as spore dispersion can affect a large area, and can still be fatal even if treatment is administered at first sign of primary symptoms [5].

Comprehensive studies of the lethality of anthrax and risk evaluation of events using anthrax have been performed by Coleman et al. These studies focus on the developing misconception that single anthrax spores can cause fatal infections. While it is possible, it is statistically unlikely, and as such the ability to predict large quantities of anthrax spores in an attack scenario is required [4]. Despite the biological studies indicating that small quantities of anthrax are unlikely to be fatal, decontamination protocols impose a zero detection tolerance for the presence of anthrax.

A complication to predicting the effects of anthrax attacks lies with the relationship between spore size and lethality. Like many bioweapons that rely on inhalation for maximum effectiveness, the size of an anthrax spore determines its respirability and therefore the potential for infection. Experiments by Druetta et al. concluded that for lab animals with similar respiratory characteristics, the lethality goes down by orders of magnitude for spore sizes increasing beyond five (5) microns [6, 7]. This results from larger spores being unable to travel effectively through the respiratory system [8]. While this size scale is not explicitly measured for model comparison in this work, the foundation to extend the model to this scale is established.

2.2 Axisymmetric Jets

A common structure encountered in fluid dynamics is the turbulent axisymmetric round jet. In this case, a fluid is injected into a host medium through a nozzle with the simplest case

being an injection into a quiescent environment where the injected fluid and host fluid are the same. In this case, the jet is the sole source of momentum introduced into the control volume, and as the jet enters the control volume it will spread with a half angle of 11.8° [9, 10]. The growth of the jet occurs in three phases: "induction", "diastrophy", and "infusion". Induction is a kinematic phase during which irrotational fluid local to the jet vorticity obtains some velocity through Biot-Savart-induction. The second phase, diastrophy, causes the fluid to gain some vorticity eventually evolving on a time scale similar to the Kolmogorov scale. The third process is diffusion based and includes such processes as molecular mixing or thermal conduction. For the case of pure gas-gas jets this phase is difficult to distinguish from the second phase especially considering that the two phases can occur at the same time. This phase is especially important when attempting to predict chemically reacting flows.

This process has been studied extensively from both experimental and simulated perspectives. Wygnanski and Fielder performed extensive analysis of these jets using hot wire anemometers to predict both a velocity profile and self-preserving characteristic length [11]. In addition, Chhabra et al. performed both simulations and particle image velocimetry (PIV) to gather further velocity profiles and entrainment characteristics [12]. Both of these studies arrived at a similar conclusion that the centerline velocity decays according to equation (1):

$$u_{cl} = \frac{B_u d_o}{x} * u_0 \tag{1}$$

where u_{cl} is the centerline velocity at any given point, x, u_o is the average velocity at the nozzle, d_o is the nozzle diameter, and B_u is the constant of decay. The constant of decay has been shown to vary with differential properties between the jet and host fluids, as well as the velocity of the host fluid, but for same fluid quiescent environments, it is approximately 5.0. This equation requires use of a specific coordinate system, where there jet is assumed to start at some "virtual point", with a nozzle position taken as $x = \frac{5d_o}{2}$.

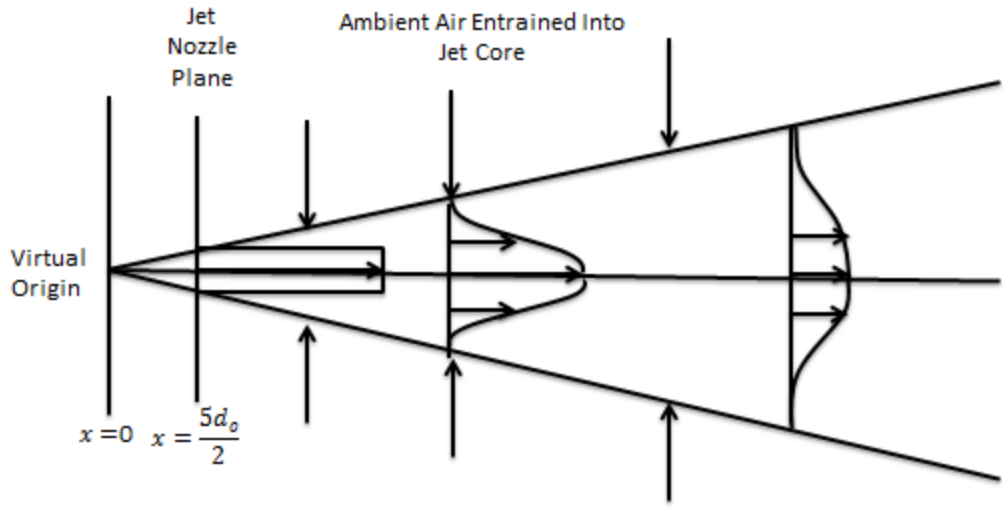

Figure 2: Development of a Turbulent Axisymmetric Jet from a Virtual Origin

2.3 Principles of Computational Fluid Dynamics (CFD)

2.3.1 General Information and Equations

For this research, the CFD program FLUENT by ANSYS, Inc. was used to create simulations of turbulent jets and particle dispersion. Like most CFD programs, FLUENT starts by solving the Navier-Stokes equations, which represent conservation of mass and momentum:

$$\frac{\partial \rho}{\partial t} + \nabla \cdot (\rho \vec{v}) = S_m \tag{2}$$

$$\frac{\partial}{\partial t}(\rho \vec{v}) + \nabla \cdot (\rho \vec{v}\vec{v}) = -\nabla P + \nabla \cdot (\bar{\bar{\tau}}) + \rho \vec{g} + \vec{F} \tag{3}$$

where S_m is a source term representing the mass added to a system through dispersion of a second phase within the flow, $\bar{\bar{\tau}}$ is a stress tensor, $\rho \vec{g}$ is a body force due to gravity, and $\vec{F}$ is any additional body force term added through interaction with a second phase or terms required for

functionality of different models. The stress tensor can be solved for using the following equation:

$$\bar{\bar{\tau}} = \mu\left[(\nabla\vec{v} + \nabla\vec{v}^{T}) - \frac{2}{3}\nabla\vec{v}I\right] \quad (4)$$

where *I* is the unit tensor and μ is the molecular viscosity.

With these equations, FLUENT can create a model predicting the flow characteristics of temperature independent laminar flows. When flows become more complicated either through the addition of thermal fluctuations or turbulence, additional equations must be added. For this research, the ambient temperature was regulated to prevent significant fluctuations in the fluid temperature, therefore energy equations were not integrated into the solver. However, due to the use of a turbulent axisymmetric jet, the use of a turbulence model was required.

2.3.2 CFD Turbulence Modeling

Due to the chaotic nature of turbulence, it is computationally expensive to calculate an exact solution to the momentum equations. In cases with simple geometries or flow characteristics, this process can be used and is called "Direct Numerical Simulation" (DNS). For cases in which the geometry is complicated or computational efficiency is required, a different approach is used. A common method is to use an averaged form of the equations presented above (2-4). In doing so, the range of scales to be calculated is reduced to the larger scales and the system is significantly less computationally intensive. The first step in this process is to decompose the variables solved in the Navier-Stokes equations into either a time or ensemble averaged component and fluctuating components. A common example is the decomposition of the velocity vector as seen in equation 5:

$$u_i = \overline{u}_\iota + u_i' \quad (5)$$

where $\overline{u}_\iota$ is the mean velocity and u_i' is the fluctuating component. This process can be applied to other scalar quantities such as pressure in the same way. If these values are introduced to the

continuity and momentum equations and an average is taken, it will produce the following ensemble averaged mass (6) and momentum (7) equations shown as Cartesian tensors:

$$\frac{\partial \rho}{\partial t} + \frac{\partial}{\partial x_i}(\rho u_i) = 0 \tag{6}$$

$$\frac{\partial}{\partial t}(\rho u_i) + \frac{\partial}{\partial x_j}(\rho u_i u_j) = -\frac{\partial P}{\partial x_i} + \frac{\partial}{\partial x_j}\left[\mu\left(\frac{\partial u_i}{\partial x_j} + \frac{\partial u_i}{\partial x_j} - \frac{2}{3}\delta_{ij}\frac{\partial u_l}{\partial x_l}\right)\right] + \frac{\partial}{\partial x_j}(-\rho\overline{u_i' u_j'}) \tag{7}$$

With the substitution of the averaged velocity variables, the equations now become less intensive to solve compared to a DNS solution. In this equation, however, a new term arises, $-\rho\overline{u_i' u_j'}$, representing the Reynolds stresses. In order to solve for this term, additional equations must be solved. Most CFD platforms give users a variety of models to solve for this added variable depending on the geometry, accuracy, and computational power available [13].

While there are many different models available for calculating turbulent solutions, these simulations in this study use the k-ε (turbulent kinetic energy and dissipation, respectively) model. There are three k-ε models available in FLUENT, which differ in how they calculate turbulent viscosity, Prandtl numbers related to the diffusion of k and ε, and the dissipation equation's generation and destruction. The first model is the Standard k-ε model, and is the oldest and simplest of the three. As a result of its age, alterations to this model have been made to improve its accuracy under certain circumstances. One of the improved models is the RNG k-ε model, which is created using "renormalized group theory", and uses different constants than the standard k-ε model as well as additional terms in the k and ε transport equations. This model can be applied to a wider variety of flow conditions, and has been adapted as an effective model for indoor airflow cases [14]. The final model is the newer "realizable k-ε model" which is capable of meeting additional mathematical constraints of the Reynolds stresses equations. This model uses a different dissipation rate transport equation based on the "mean-square vorticity fluctuation". This new equation allows the realizable model to consistently outperform both the

standard and RNG models when computing cases with round jets and for this reason was selected as the turbulence model for this research.

2.3.3 Multiphase Particle Modeling: Eulerian verses Lagrangian Tracking

In multiphase particle CFD modeling, there are two commonly used approaches: the Eulerian model and the Lagrangian model. The models differ by their treatment of the second particle phase. The Eulerian model treats the particle phase as a second continuum phase calculated from mass conservation principles [15]. In this case, the solution is typically interpreted in terms of a concentration field, since individual particles cannot be tracked in this method. The Lagrangian model differs from the Eulerian model in that it treats the second phase as a discrete collection of individual particles. The trajectory of each particle is calculated based on Newton's Second Law where the momentum imparted comes from the interaction with the continuous phase as well as particle body forces. The primary forces considered are drag forces, pressure gradient forces, Basset forces, virtual (added mass) forces, Brownian forces, gravitational forces, and buoyancy forces [16]. While this is not a complete list of forces, cumulatively, they comprise a high majority of forces which can affect particle trajectories. The resultant force is then calculated at discrete time intervals and the particle is advanced according to the force. This is why the Lagrangian model is sometimes referred to as the "discrete phase model". The nature and effect of these forces will be discussed in greater detail in section 2.4.

Each model has specific advantages and disadvantages depending on the requirements of the simulation. For cases in which a concentration field is the main priority, the Eulerian model is preferred since its method of calculation innately generates a concentration profile. In contrast, a case study in which concentration is not the primary concern, but rather particle history is desired, the Lagrangian model is preferred; although a concentration can be generated from Lagrangian data, it requires additional post processing [17]. In terms of efficiency, the Eulerian model requires significantly less computational power since it solves for a single continuum, while the Lagrangian model must solve for multiple independent particle trajectories. This gives rise to another issue with Lagrangian tracking; a large number of particles must be tested in order to generate a statistically reliable solution. Given these characteristics, there are specific scenarios in which each model is preferred. In many simulations of particle dispersion with larger heavy particles ($\rho_{particle} >> \rho_{fluid}$), Lagrangian models are used because the particle

behavior is significantly different from that of the continuum phase due to the effects of gravity and buoyancy [18]. When smaller particles (below the Kolmogorov microscale) are simulated, the Eulerian model is often used because the particles behave more like flow tracers and obtain motion similar to a second continuum phase [17]. Furthermore, studies comparing the two models when particle injections occur during flow field development conclude that the Lagrangian model tends to produce more reliable results due to its ability to predict more of the flow and particle physics [19, 20]. Since this research focuses on both heavy particles and tracking where the particle history is of high importance, the Lagrangian method will be used.

2.4 Principles of Particle Dispersion

Particle dispersion can be separated into three unique operations: mixing, spreading, and bulk transport. Mixing is the process of generating a homogenous mixture, typically of two or more particle streams. Spreading occurs when particles move into regions unoccupied by particles where particle concentration will decrease as spreading occurs. The final method is bulk transport of particles from one region to another. While each of these types of dispersion can occur separately, in the case of particle laden jets, all three occur simultaneously [21].

When calculating particle dispersion using the Lagrangian model, many different forces must be calculated simultaneously in order to produce the resultant trajectory vector for a specific time step. The motion of a particle in a dilute multiphase flow is driven by the lift and drag forces imparted to the particle from the continuous phase. As was stated previously, these forces can be broken down into drag, pressure gradient, Basset/Virtual Mass, Brownian, and Body forces, which comprise a list of some of the most significant forces acting on a particle. While these forces may cumulatively have a high impact on particle trajectory, the extent to which each force controls the motion of the particle is dependent on many factors including particle size and density.

2.4.1 Particle Reynolds Number and Regime Definition

When discussing particle dispersion, the first step in defining the process is to determine the dominant forces acting on a particle. Particles are classified as being within the Stokes regime (dominated by viscous forces), Newtonian regime (dominated by inertial forces), or Transitional regime (a combination of the two). This classification is typically done by defining the particle Reynolds number found in equation (8):

$$Re_p = \frac{dV_s}{\nu_c} \tag{8}$$

where V_s is the characteristic settling velocity of a particle, which is defined by equation (9) for smaller particles falling in the Stokes region:

$$V_{s,Stokes} = \frac{2(\rho_p - \rho_c)gr^2}{9\mu_c} \tag{9}$$

For larger particles (Re_p>1), classified in either the Newtonian or Transitional regions, the settling velocity is defined by equation (10).

$$V_{s,Newtonian} = \left(\frac{4\rho_p g d}{3C_D\rho_c}\right)^{\frac{1}{2}} \tag{10}$$

Determining which regime a particle is classified in will determine which method for determining the drag coefficient must be used [22].

2.4.2 Drag Forces

One of the simplest forces involved in multiphase flows is the drag force. The standard form for determining the drag force is:

$$F_D = C_D \frac{\pi}{8}\rho_c d^2 V^2 \tag{11}$$

where C_D is the drag coefficient, ρ_g is the density of the continuous phase, d is the particle diameter, and V is the particle velocity. The drag coefficient, C_D, changes with relation to particle and flow characteristics. It remains approximately constant ($C_D \approx 0.44$) for large particles (Re_p >1000) as the inertial effects of the particle are dominant in this range. This region is often referred to as the "Newtonian Region". At the other extreme, very small particles (Re_p<1), the assumption is made that inertial effects of the particle are negligible compared to the magnitude of viscous forces. In this case, the drag coefficient takes on the form:

$$C_D = \frac{24}{Re_p} \tag{12}$$

For particles where $1<Re_p<1000$, experimentation has shown the drag coefficient is expressed by equation (13) [22].

$$C_D = \frac{24}{Re_p}(1 + 0.15Re_p^{0.687}) \tag{13}$$

2.4.3 Lift Forces

When determining lift forces of a particle within a continuum, there are typically two types of lift addressed: the Saffman Lift Force and the Magnus Lift Force. In the case of the Saffman force, a shear lift force is generated by a differential pressure distribution on a particle caused by a velocity gradient. The magnitude of this force was determined to be:

$$F_{saff} = .161\mu_c d|u_i - v_i|\sqrt{Re_g} \tag{14}$$

where μ_c is the carrier fluid dynamic viscosity, d is the particle diameter, $|u_i - v_i|$ is the particle-fluid differential velocity, and Re_g is the shear Reynolds number defined as:

$$Re_g = \frac{d^2}{\nu_c}\frac{du}{dy} \tag{15}$$

This force is negligible unless the particle Reynolds number is less than one [23].
The Magnus Lift Force results directly from the rotation of a particle moving through a carrier fluid. The magnitude of the Magnus force can be calculated using equation 16:

$$F_{mag} = \frac{\pi}{8}d^3\rho_c\omega_d(v - u) \tag{16}$$

Unlike the Saffman Lift Force, the Magnus force is typically applied to larger particles ranging from the millimeter scale to objects such as baseballs and golf balls [24]. The scale of particle sizes of interest will determine which of the two lift forces is of greater importance.

2.4.4 Virtual Mass and Basset Forces

In addition to the standard lift and drag forces, a category of forces arises from the relative acceleration of a particle within a fluid; these forces are the Virtual Mass and Basset forces. The Virtual Mass force arises from the particle causing acceleration in the surrounding fluid; this creates an added drag force relative to the mass of the fluid displaced. The magnitude of this force can be determined using equation 17:

$$F_{vm,i} = \frac{\rho_c V_d}{2}\left(\frac{Du_i}{Dt} - \frac{dv_i}{dt}\right) \tag{17}$$

where V_d is the volume of the displaced fluid.

Much like the Virtual Mass force represents additional drag on a particle as a result of acceleration in a fluid, the Basset force represents additional forces that arise from viscous effects. The force is directly related to the lag time in the development of the boundary layer during the particle's velocity change. The Basset force can be calculated using equation 18:

$$F_{Basset,i} = \frac{3}{2} d^2 \sqrt{\pi \rho_c \mu_c} \int_0^t \frac{\frac{d}{dt'}(u_i - v_i)}{\sqrt{t - t'}} dt' \tag{18}$$

Since this equation contains a time integral, it is often referred to as the "history term", as it describes the force acting on the particle throughout any transience in its acceleration [16]. Experimentation has concluded that for density ratios $\frac{\rho_c}{\rho_d} \sim 0.001$, the effect of the Basset and Virtual Mass forces become insignificant [25]. In addition, experimentation and simulations demonstrate that the Basset and Virtual mass forces have little to no effect on fluctuations in the fluid velocity capable of altering the trajectory of any entrained particles [26].

2.4.5 Brownian Forces

Brownian motion is a phenomenon that arises when small particles interact with another medium on the atom level. A particle suspended in a fluid will be constantly subjected to the

random bombardment by the atoms and molecules that comprise the fluid. Since it is statistically unlikely that these collisions will occur at offsetting locations on the particle at the same time, they impart some of their kinetic energy to the particle, which in turn causes some motion. This process is referred to as a continuous-state-space first order Markov process. This means that, in a discrete domain, current properties of the particle are solely dependent on the state in the most recent discrete time step. In the case of position, x(t), it is dependent only on x(t-Δt), where Δt is some chosen discrete time step [27].

Since this process is not strictly a continuum interaction of particle to phase, it is typically modeled as a statistical process. In the case of Brownian motion, FLUENT utilizes a Gaussian white noise random process with a coefficient of spectral intensity calculated using equation 19:

$$S_o = \frac{216\nu kT}{\pi^2 \rho_c d^5 S^2 C_c} \tag{19}$$

where S is the ratio of particle density to fluid density, k is the Boltzmann constant ($1.38\text{x}10^{-23}$ J/K), and C_c is the Stokes-Cunningham Slip Correction factor which compares the scale of the particle to the atomic mean free path of the fluid. This coefficient can then be used to determine the magnitude of the Brownian Force using equation 20:

$$F_{Brownian} = G_i \sqrt{\frac{\pi S_o}{\Delta t}} \tag{20}$$

where $G_i$is a randomly distributed variable with a mean of zero and a variance of unity. The effects of Brownian motion are of the most significance when the Knudsen number is of order unity, meaning the particle is a size similar to the scale of the mean free path of the fluid [28].

2.4.6 Comparison of Forces (Body Forces)

Studies to determine the entrainment characteristics of individual particles are based on solving the balance of these forces. For a typical entrainment process, the forces of lift and buoyancy must be greater than the force of gravity and adhesion (in the case of entrainment from a static surface position). Experiments in pick-up velocity within a pneumatic transport system indicate that the two dominant forces on a particle are gravity and lift, both increasing

significantly with increases in particle size [29, 30]. The relationship between particle size and the nature of the forces is often broken down into three regions: 1) Large particles where inter-particle forces (i.e. cohesion) are negligible, 2) Smaller particles where inter-particle forces are significant but are not the dominant force can cause individual particles to entrainment even in the presence of agglomerates, 3) Small particles where inter-particle forces are strong enough to cause entrainment of agglomerates [31].

2.5 Particle Characteristics and Flow Interaction

2.5.1 Stokes Number and the Kolmogorov Microscale

When discussing particle dispersion, there are many different characteristics that contribute to defining the particle geometry and the relationship of the particle to the flow. One of the most commonly used particle characteristics is the Stokes Number (St), which quantifies the ratio of the aerodynamic response time (otherwise called the relaxation time) of a particle to the characteristics timescale of a structures flow. The Stokes number for a system can be calculated using equation 21:

$$St = \frac{\rho_p d^2 U}{18 \mu \delta} \tag{21}$$

where δ is the characteristic length of the structure of interest. In cases involving free jet structures, this value can change with location but is often taken as the nozzle diameter as an initial estimate [32]. The Stokes number can be used to categorize different behaviors of particles within flows. For example, particle flows with a Stokes number less than 1 tend to act as flow tracers, since the particle response time is sufficiently low, it allows the particles to rapidly change direction within the flow structure. For cases in which the Stokes number is approximately 1, the particles have similar behavior, however, they will show some lagged behavior to the flow streamlines [33, 34]. In the case of larger Stokes number (St>>1), the aerodynamic response time is sufficiently large such that the particle is not significantly affected by the fluctuations in the flow field and will tend to follow a more rectilinear path.

In addition to the Stokes number, a useful parameter of the flow in determining particle dispersion is the Kolmogorov microscale. The Kolmogorov scale is used to determine the scales

at which turbulent energy dissipation occurs, and is especially important for cases with very high Reynolds numbers. The Kolmogorov microscale is defined in equation 22:

$$\eta_k \equiv \left(\frac{\nu^3}{\varepsilon}\right)^{\frac{1}{4}} \tag{22}$$

where ε is the average energy dissipation per unit mass. Estimating η_k can be done by relating the Reynolds number of the flow using equation 23:

$$\frac{\eta_k}{l} = Re_l^{-\frac{3}{4}} \tag{23}$$

where $Re_l$is the turbulence Reynolds number and l is the scale at which energy containing eddies form[35]. This scale can then be compared to the particle size. For cases in which the particle size is on the same scale as the Kolmogorov microscale, particle behavior is similar to that of tracer. In addition, computational accuracy can be assessed based on the Kolmogorov scale. A mesh grid spacing should be on a similar magnitude as the Kolmogorov scale in order to accurately capture the smallest scales of turbulence for cases in which particle size is of the order of the Kolmogorov scale [36].

2.5.2 Stopping Distance

Studies have indicated that a useful parameter in determining entrainment properties in jets is the stopping distance. The stopping distance is defined as the distance a particle with some initial velocity will travel in a quiescent environment and for a Stokes regime particle can be calculated using equation 24:

$$\lambda = \frac{2r^2 V \rho_p}{9\mu} \tag{24}$$

In some cases involving jets, this value is made non-dimensional by dividing by the nozzle diameter because a common assumption with free jets is to take the characteristic eddy size as the nozzle diameter. The value of the stopping distance can be divided into three regions in which the nature of the particle and fluid interaction change. The smallest values for stopping distance describe a region in which the particles have a low Stokes number and cause the fluid to behave as an ideal gas only with a higher molecular weight. As the stopping distance increases, the particles have a damping effect on the turbulence of the jet structure, which will decrease the amount of quiescent fluid entrained into the jet. The largest scale shows little to no interaction between the flow and the particle because the time scale of the momentum transfer is significantly larger than the scale at which the jet mechanics occur [37].

2.5.3 Poly-disperse versus Mono-disperse Particle Characteristics

When measuring particle dispersion of large numbers of particles, the distribution of particle shape and size can have significant effects on the distribution of particles in turbulent structures. The dispersion coefficient of a particle set is determined by the ratio of the standard deviation to the mean and follows the form $\frac{\sigma}{\mu} < 0.1$ for mono-disperse particle groups [16]. This factor becomes especially important for "heavy" particles which can introduce the "poly-disperse sedimentation effect" when particles enter free fall in a quiescent environment. Due to the differential in size, larger particles will tend to fall at a higher rate causing an increase in the dispersion in the vertical direction. This can be accounted for by using correction factors, but in experimentation and simulation cases it is often advised to simply ensure that mono-dispersed particle samples are used instead [38].

2.5.4 Phase Coupling

When determining particle entrainment characteristics, the level of interaction between the particle phase and the fluid phase must be determined. This interaction is typically broken into a series of "coupling" scenarios: 1-way coupling, 2-way coupling, and 4-way coupling. The first scenario occurs during very low particle loading cases, in which the effect of dispersion is dominated by turbulent effects while the transfer of momentum from the particles to the flow is not significant due to the low concentration. The second case arises when the particle loading is sufficiently high that there is enough momentum transfer between the particles and the turbulent phase in addition to the standard interaction of the fluid to the particles. This region can be

further divided into ranges in which the effect on turbulence is dampening or enhancing. For cases in which the Stokes number of the particle is small, the added surface area allows a higher level of momentum transfer, thereby dissipating the turbulence (i.e. acts as a damper). Larger diameter particles can introduce additional vortex shedding and add to the turbulent energy produced [39]. In the two-way coupling regime, there is an additional relationship between Stokes number and jet stability. It has been shown through experimentation ([40, 41]) as well as numeric simulation ([42, 43]) that particles with a small Stokes number tend to cause jet instability while larger Stokes number particles have a stabilizing influence on turbulent flows. The final scale encompasses both the fluid's effect on the particles and the particle's effect on the fluid, but also introduces the effect of particle collisions. This phase is typically only encountered for very dense flows where a granular effect becomes significant.

Chapter 3: Simulation Parameters

The modeling of the companion experiment described in chapter 1 was broken into two unique aspects: the injection system and a free jet penetrating an otherwise controlled quiescent environment. The two geometries were simulated separately in order to produce results in a timely manner with the computational resources available.

3.1 Injection System

3.1.1 Model Geometry

This section details the geometry and simulation details of the injection system used to introduce particles into a turbulent jet. The system consists of a 1" PVC pipe connected between an analog flow meter and a 2" PVC pipe. The 2" PVC pipe has an added segment angled at 45° designed to add particles to the flow. The setup can be seen in greater detail in figure 3 below.

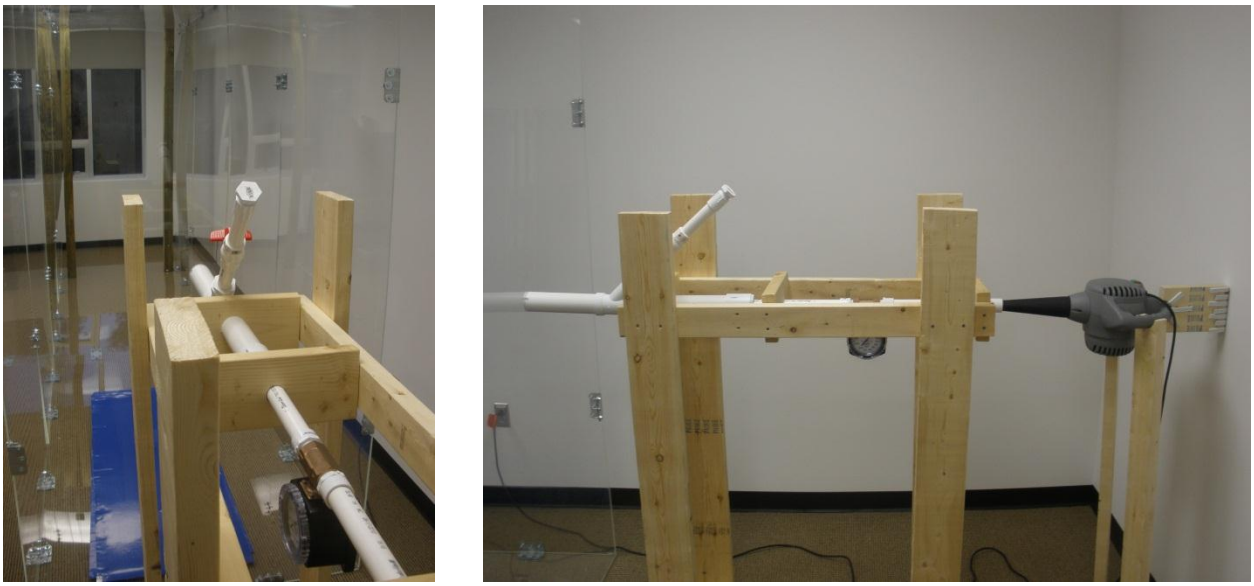

Figure 3: Particle Injection System

In order to determine the difference (if any) this system would introduce compared to a standard free jet with particle injection occurring directly at the nozzle, a simplified version of the system was modeled using FLUENT. The quiescent environment modeled as a wind tunnel and the injection system were modeled separately in order to simplify the system geometry and work with the computing power available. The injection system model was evaluated for both flow and particle characteristics. In order to avoid any potential error introduced by the flow meter,

the simulated geometry begins at a point immediately following the outlet of the nozzle. Experimentation using a Pitot tube anemometer indicated that the in line flow meter caused a significant loss of mass flow across the device and produced an inlet velocity of 59 m/s compared to the flow meter value of 130.4 m/s (derived from a flow rate of 140 ft^3/min through a circular inlet with a 1 in diameter). The assumption was made that the flow meter was placed at a sufficient distance downstream from the nozzle as to allow fully developed flow, and in order to check this assumption, the velocity profile of the injection system was analyzed at the nozzle exit (entrance into the quiescent environment).

The injection system geometry was created using simple extrusions and revolutions based on the measurements taken from the physical system and can be seen in greater detail in Figure 4:

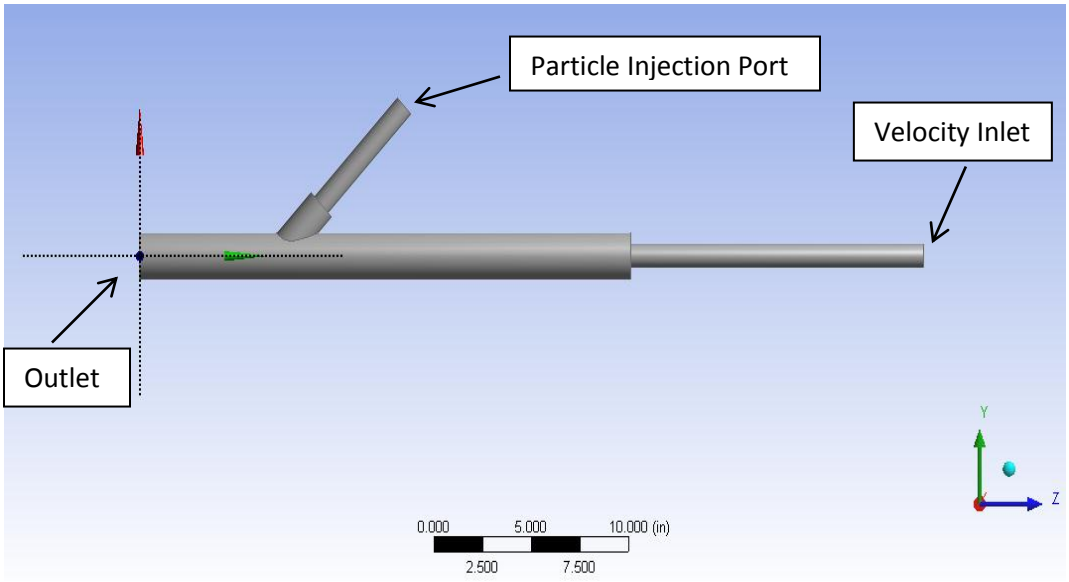

Figure 4: FLUENT Modeled Injection System Geometry

3.1.2 Injection System Meshing

The geometry was meshed using the FLUENT option "Advanced Sizing Function: Fixed" to create variable element sizes in order to create multiple levels of refinement to test for grid independence (the condition where the shape or level of refinement of a mesh has no significant effect on the solution). Additional details of the grid independence study can be found in Chapter 5. Due to computational power limitations, the finest mesh contains 400,000 nodes and can be seen below in Figure 5.

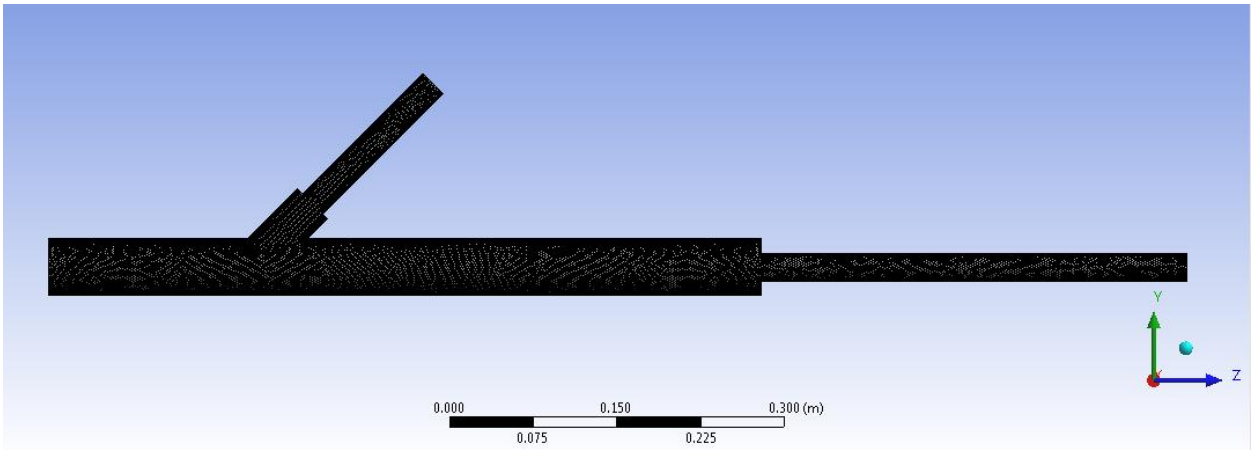

Figure 5: Injection System Mesh (Finest)

The system was modeled using a steady state Realizable k-ε turbulence model in order to solve for the flow field characteristics. The Realizable model was used to better predict the jet like behavior that arises from the changes in diameter of the pipes, while a steady solution was used to better reflect the experimental condition of waiting until the air supply had stabilized (as read by the flow meter). A convergent solution was determined through the decay of the residuals determined by FLUENT, with a minimum required drop of 2 orders of magnitude and long term stability (minimum fluctuations between iterations).

3.1.3 Injection System Particle Tracking

In order to better understand the effect the injection system has on particle distribution, particle injections was created using the Discrete Phase Modeling (DPM) Lagrangian tracking scheme at the surface labeled "Particle Injection Port" in Figure 4 for the particle sizes and densities detailed below. The injections were modeled after experimental measurements of the diameters of the various particles to determine both the difference (if any) from manufacturer's specified diameters as well as the standard deviation of the particle diameters in order to determine any poly-disperse characterization. The values of these measurements can be seen below in Table 1:

Table 1: Particle Information Overview

Material Type:	Glass	Glass	Glass	Glass	Chrome Steel	Zirconia-Silica	Zirconia
Material Density (kg/m^3):	2500	2500	2500	2500	7900	3700	5500
Proposed Mean Particle Diameter (mm):	6.4	3.0-3.5	2.5	1.0	2.3	1.0	1.0
Measured Mean Particle Diameter (mm):	5.995	3.646	2.602	1.168	2.383	1.121	1.072
Standard Deviation (mm):	0.084	0.178	0.148	0.096	0.009	0.068	0.072
Dispersal Coefficient:	0.014	0.049	0.057	0.082	0.004	0.061	0.067

As can be seen in Table 2, all of the particles fall into the mono-disperse region as discussed by Crowe et al and are not likely to be significantly affected by the poly-disperse sedimentation effect despite the larger diameters and high densities. In order to determine which additional body forces, if any, must be accounted for, the Particle Reynolds number for each case must be calculated using equations (8-10). The results of these calculations can be seen in Table 2 below.

Table 2: Particle Reynolds Number and Regime

Material Type:	Glass	Glass	Glass	Glass	Chrome Steel	Zirconia-Silica	Zirconia
Measured Diameter (mm):	5.995	3.646	2.602	1.168	2.383	1.121	1.072
Particle Settling Velocity (m/s)	19.236	15.001	12.673	7.699	21.561	9.455	11.606
Particle Reynolds Number	7354.451	3487.721	2102.927	573.234	3277.177	675.701	793.619
Particle Regime	Newtonian	Newtonian	Newtonian	Transitional	Newtonian	Transitional	Transitional

For the cases of the smallest glass, Zirconia-Silica, and Zirconia particles, the equations were solved starting with the Newtonian assumption of $C_D = 0.44$. A Particle Reynolds number below 1000 was calculated, indicating transitional flow. Since the value of the drag coefficient changes within this region in relation to the Particle Reynolds number as seen in equation 13, an iterative solution was devised. In each of these cases the particle Reynolds number is significantly greater than 1 and as such is firmly outside the Stokes Region. Given the Particle Reynolds numbers calculated, the magnitude of forces such as the Brownian force can be ignored in relation to lift, drag, and gravitational forces.

In order to produce the most accurate solution, the particle volume fraction was determined using the total volume of the injection system and an injection of 100 particles (experimental standard). The largest volume fraction (based on the 5.995mm diameter glass) was calculated to be on the order of 10^{-3} indicating that the particle injection has measurable effect on the flow. For this reason the particle tracking scheme used within the injection system utilized a "two-way phase coupling" as was previously discussed. In addition, since the Lagrangian tracking scheme was used, a large number of runs were required. Since the default surface particle injection system is

limited to a single particle for each meshed element on that surface, a Stochastic tracking function was added. In this process, particles are staggered spatially in order to achieve a higher utilization of the surface and allowing for a higher number of particles to be tracked without significantly increasing the computational requirement. A sample of the particle injection tracking scheme using the 1mm glass particles can be seen below in Figure 6. The particles fall under the force of gravity from the injection surface, and are entrained into the flow before exiting at the nozzle.

The particle interaction with the walls of the injection system was controlled using the "reflect" boundary condition on all exterior faces of the mesh except those define in Figure 4. In doing so, any particle collision with the walls will alter the trajectory of any particle according to its coefficient of restitution. The values for the coefficients of restitution were determined though simple experimentation by measuring the ratio of the initial height of a particle to the height after one impact with a surface of material similar to that of the PVC pipe. This test showed that the values for all sizes of glass particles were nearly identical at 0.65. The chrome steel was slightly lower at 0.50, while the Zirconia and Zirconia-Silica were in between at 0.55 and .60 respectively. These values were passed into FLUENT as constant coefficients of restitution for each case for both the normal and tangential components of the reflection behavior.

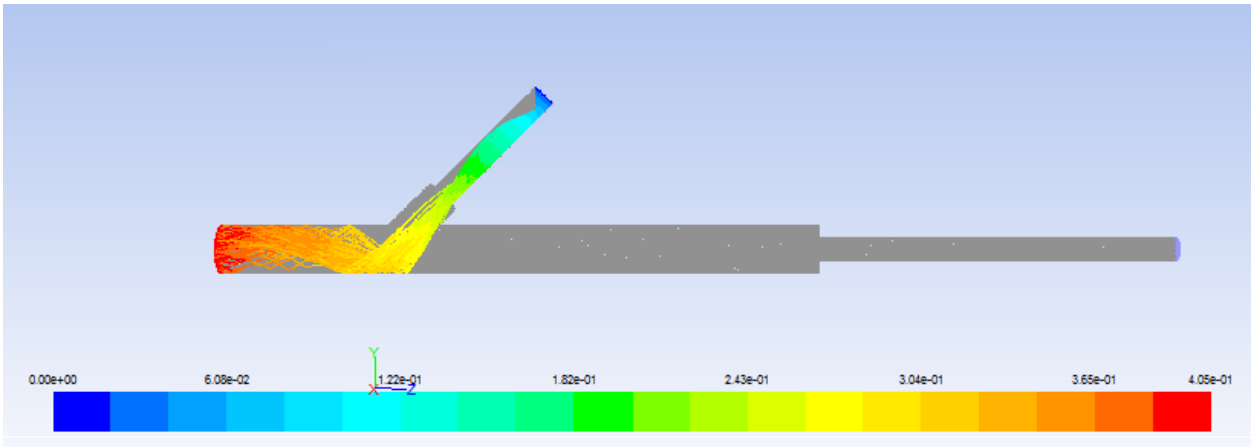

Figure 6: Sample Particle Injection Tracking (1mm glass) Color Coded by Particle Residence Time (s)

3.2 Quiescent Environment (Wind Tunnel)

3.2.1 Wind Tunnel Geometry

In order to produce results usable as a baseline for future investigation, a controlled quiescent environment was created using large panels of Plexiglas to create a wind tunnel measuring 4 feet in width, 8 feet in height, and 16 feet in length with a 2 inch jet nozzle at one end and an open pressure outlet at the opposing end. This was modeled in FLUENT using wall conditions for the boundaries with the exception of the end wall which was modeled as a pressure outlet venting to the atmosphere (i.e. zero gauge pressure). Upon initial simulations and experimental results, the size of the control volume and the need for a fine mesh to effectively measure the domain required a change in the geometry used.

Preliminary experimentation demonstrated that, for the particle sizes and densities tested, the highest average distance traveled by entrained particles was approximately 54 inches (1.372 m) for the 1.121 Zirconia-Silica particles. In order to allow a mesh with sufficiently small elements, the overall length of the tunnel was shortened from 16 feet to 10 feet.

3.2.2 Wind Tunnel Meshing

Similar to the injection system, an "Advanced Sizing Function: Fixed" condition was used to create the mesh for the wind tunnel. In this case, an additional face sizing feature was added to the velocity inlet in order to provide a higher level of accuracy for both initialization purposes and to allow for a higher accuracy for initial particle injection. Initial testing indicated that a coarse mesh at the inlet provided significant error in the initial velocity in the core of the jet structure. This error could propagate as the simulation ran, producing results that are unreliable. As was the case with the injection system, a variety of mesh sizes were tested in order to test for grid independence; the finest mesh tested contained 400,000 nodes and can be seen below in Figure 7.

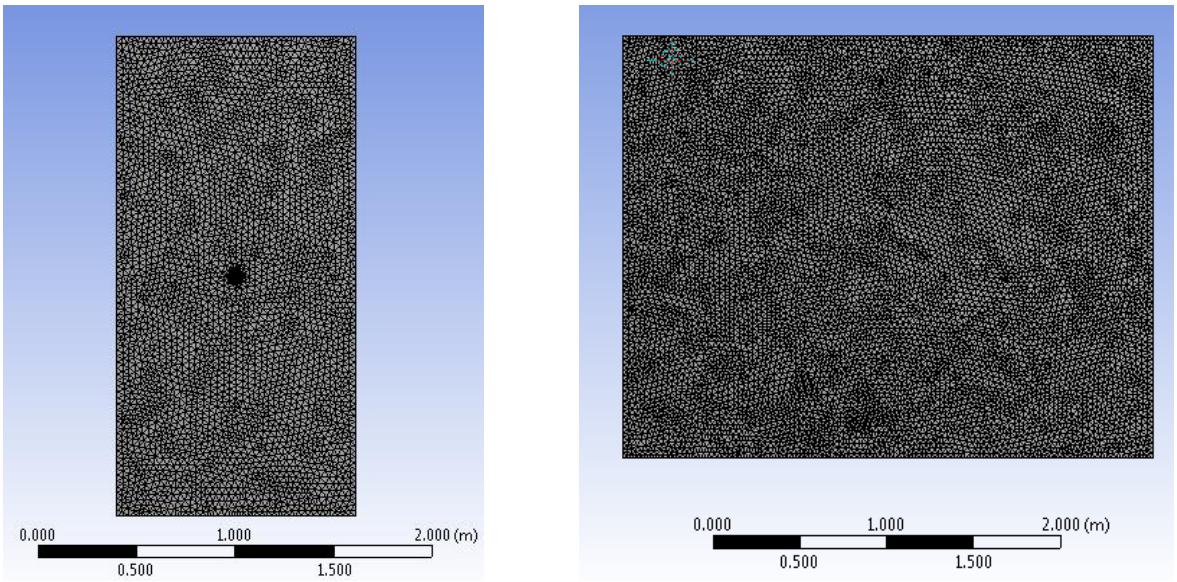

Figure 7: Wind Tunnel Mesh (Finest)

3.2.3 Wind Tunnel Particle Tracking

The Lagrangian tracking scheme was used again for this stage of the simulation using the same sample of particles as discussed in section 3.1.3. As was the case with the injection system, the particle volume fraction was calculated in order to determine the effect of phase coupling. In order to determine the most conservative estimate of the volume fraction, only the volume of the core jet structure (a canonical shape with an 11.8° angle and a height of 10 feet) was used to determine the volume fraction. A sample, simulated flow field visualization of this structure can be seen in Figure 8. In this figure, the fluid entrainment into the core structure can be seen as well as the spreading angle. In this case the spreading half angle was measured along the initial core structure, and was approximately 12°, agreeing well with the theoretical and experimental studies on turbulent axisymmetric jets. In addition, the vector plot shows the characteristic entrainment of fluid into the jet core causing the growth in the shear layer with relation to distance from the nozzle.

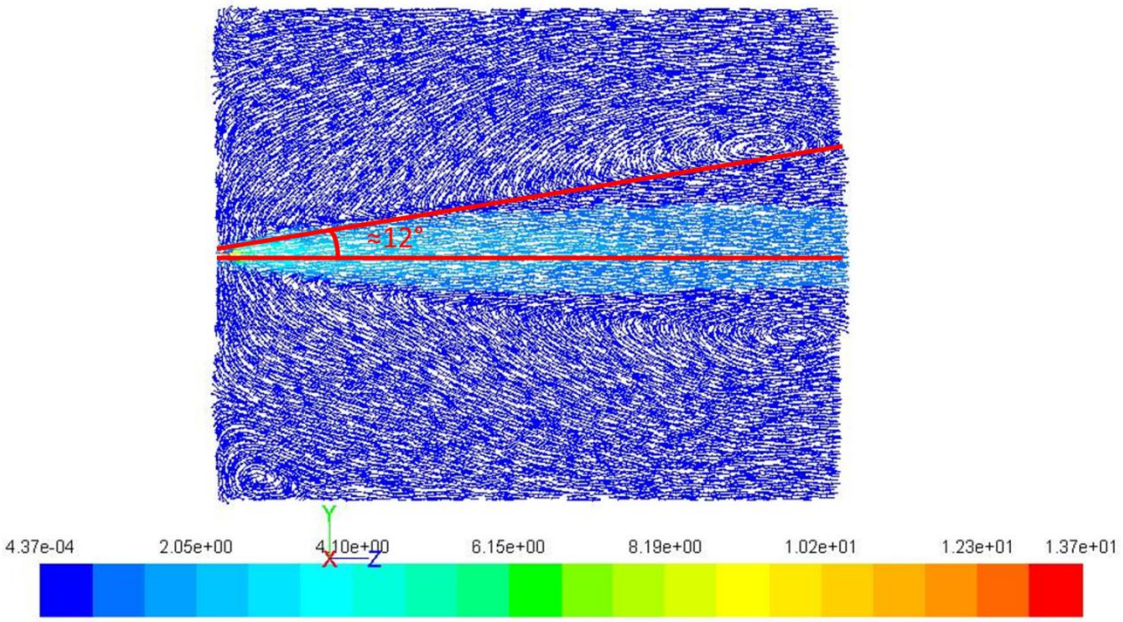

Figure 8: Wind Tunnel Simulation Result Showing Jet Core Velocities (m/s)

Using this characteristic volume, the volume fraction for a loading of 100 particles (experimental standard) of 5.995 mm glass produced a volume fraction on the order of 10^{-8}, placing it firmly within the one-way coupling region.

Chapter 4: Initial Simulation and Experimentation

4.1 Impinging Jets in Confined Environments

One of the first investigations into turbulent jets and entrainment properties used a simple cube with a velocity inlet centered on the top plane with outflows centered on the sides of the geometry. The physical model can be seen below in Figure 9, where an added support structure was constructed in order to provide stability to the flow source.

Figure 9: Impinged Jet Box Experiment

The purpose of this experiment was to determine what effect (if any) particle size has on the entrainment into a turbulent structure, in this case the impinging jet. As can be seen in the figure, particles are loaded on the bottom surface of the control volume; note that in this figure a test was being performed to simulate a large particle size fluidized bed while a normal set-up would consist of only a single layer of particles. The model consisted of a 1 ft^3 cube with 2 inch diameter circular inlets centered as described.

The flow field was modeled using the Realizable k-ε turbulence model assuming a uniform initial inlet velocity of 30 m/s (estimated based on air supply specifications and flow meter measurements). The flow field was examined by looking at the center plane of the box, aligned to show both of the outlets. This flow field can be seen below in Figure 10. As expected, the jet

impinges upon the bottom of the control volume, creating a symmetric flow pattern about the central stagnation point. The recirculation from the bottom plane is the mechanism by which particles are entrained into the flow and, depending on the trajectory of said particles, escape through one of the centered outlets on the side of the box.

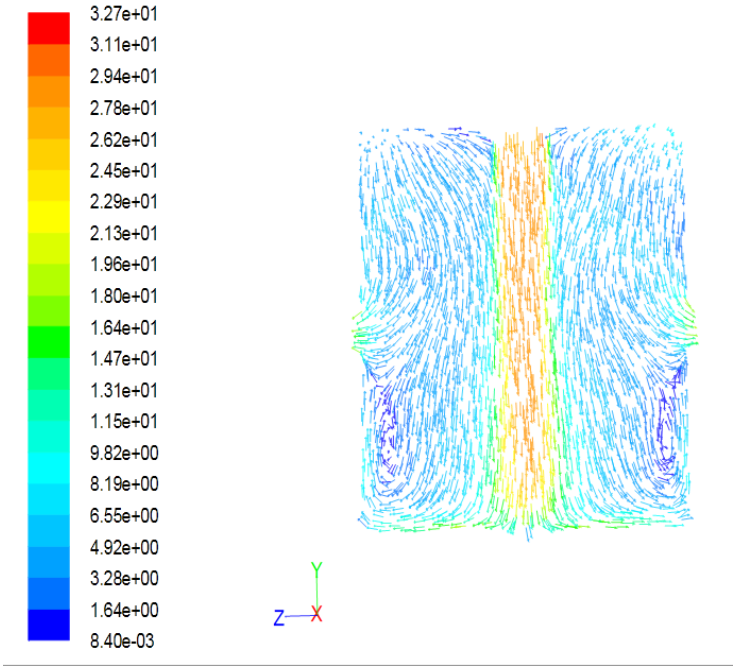

Figure 10: Box Experiment Center Plane Velocity Flow Field (m/s)

4.2 Particle Dispersion Simulation Results

Surface injections using different particle sizes were created on the bottom plane of the control volume in order to test dispersion patterns of the particles in relation to their size. The primary proof of concept particle used was standard industrial airsoft pellets with a diameter of 6mm and a density of 1060 kg/m^3. In this test, particles failed to entrain in the upward currents, and instead were carried along the floor of the box to the four corners of the domain where stagnation points developed. This same behavior was seen in the simulation using the Lagrangian tracking scheme. In order to advance experimental runs, simulations were carried out using progressively smaller particle diameters (holding density constant) in order to determine a minimum particle size for entrainment to occur at the specified conditions.

In order to measure the magnitude of entrainment, the percent evacuation of particles from the control volume was calculated for each particle size. The primary concern with this method was the manner in which FLUENT exports particle status as "escaped" (crossing one of the pressure outlet boundaries) or "incomplete" (still within the control volume). In order to eliminate this problem, for any cases which reported particles as "incomplete", the number of time steps used by the discrete phase model was increased by 10% and the particle tracking solution was run again. This was done until no change in the number of particles marked as "incomplete" was observed. With the number of particles marked as "incomplete" not changing, the position of these particles was inspected using a particle tracking display. In each case evaluated, the "incomplete" particles had become trapped in circulating loops or at stagnation points.

With the final fate of each particle determined for various sizes, a plot was generated to compare the particle size to the percent evacuation from the chamber which can be seen in Figure 11.

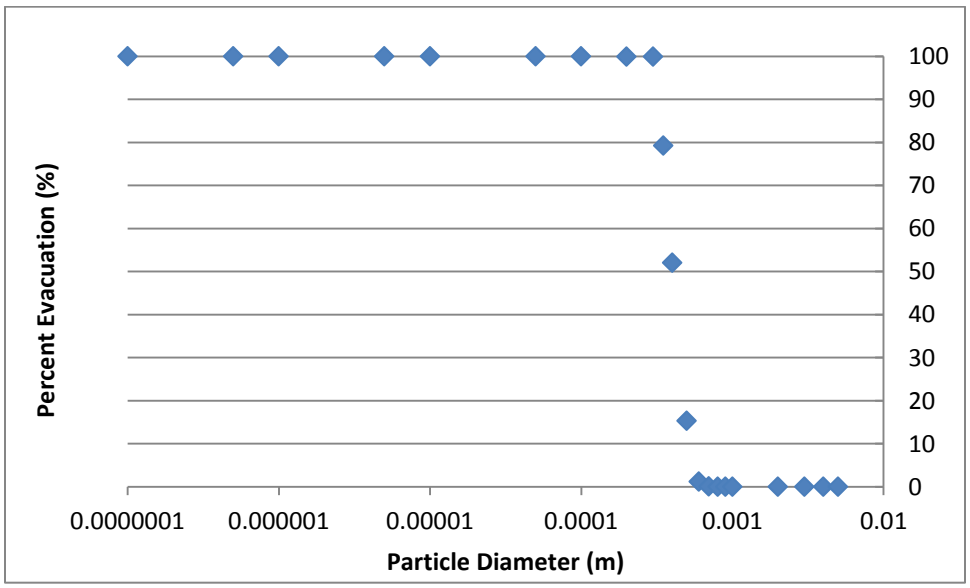

Figure 11: Box Experiment Particle Size Percent Evacuation Relationship

This plot shows a rapid change in the magnitude of entrainment experienced by particles based on particle size with the first particle of significant evacuation being 0.5mm in diameter. A more detailed view of the change on a linear scale can be seen in Figure 12.

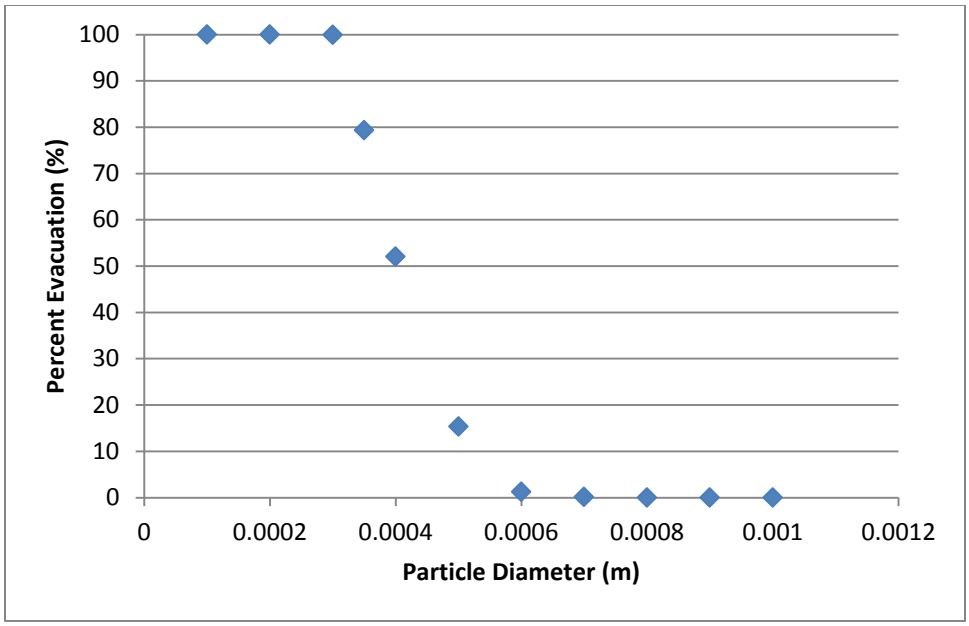

Figure 12: Particle Evacuation Focused View

The .5mm particle would have a Particle Reynolds number of approximately 64.94, placing it within the transitional region of particle regimes. Furthermore, the particles which show 100% evacuation are all 0.1mm ($Re_p \approx 1.6$) or smaller meaning the point of total evacuation borders between transitional and Stokes particle flow.

This scale can be compared to the Kolmogorov microscale of the system. Using equations (22) and (23), the microscale was calculated to be 0.761mm for an inlet velocity of 33 m/s and a characteristic length of 0.0508m. This means that the particles have the greatest level of interaction with the flow at sizes below 0.761mm which fits with the model's prediction of increasing levels of entrainment at particle diameters of 0.5mm and smaller.

Chapter 5: Simulation Analysis

In order to ensure the highest quality results from the simulations discussed series of grid independence studies were conducted. Using the fixed advanced sizing function, the cell size was lowered in order to double the number of nodes used in the simulation.

5.1 Injection System Grid Independence

Since the injection system focused on producing a variety of results for implementation in later simulations, an effective grid independence study was required in order to ensure that the results were accurate. This was accomplished by initially creating a series of 4 meshes of increasing number of nodes starting with 100,000 nodes. This simulation was evaluated for flow characteristics including overall pipe centerline velocity and nozzle velocity profile. Using the fixed sizing function, the average cell size was reduced by a factor of 2 (approximately doubling the number of nodes) and the simulation was run again. This process was repeated two more times to produce meshes of 400,000 nodes and 800,000 nodes. It is important to note that the simulating utilizing the 800,000 node mesh was never carried to completion due to computational limitations producing an estimated completion time on the order of 30+ days.

Using the first three mesh sizes, the flow characteristics were compared in order to determine the effect of any discretization error from mesh coarseness. The first comparison was of the centerline velocity of the injection system. The overlaid centerline velocities of each case can be seen in Figure 13. The plot shows that for the coarsest mesh case, there are significant fluctuations in the velocity at the change in pipe diameter and around the point where the 45° injection tube joins the geometry. By comparison, the medium and fine meshes show little fluctuations and are nearly identical.

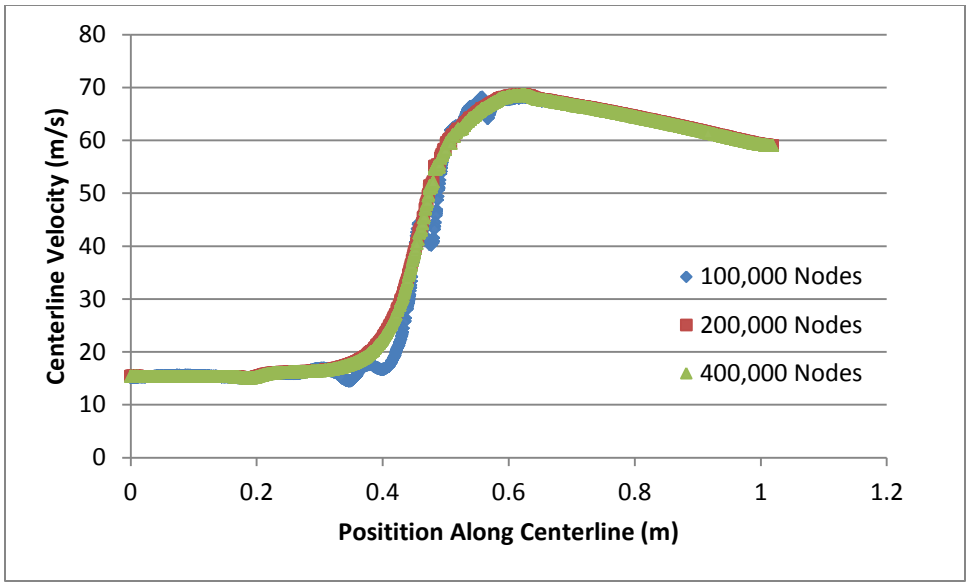

Figure 13: Comparison of Centerline Velocity of Injection System for Different Mesh Refinements

In addition to the centerline velocity, the vertical nozzle velocity was measured at the center of the outlet and can be seen in figure 14. As was the case with the centerline velocity, the coarsest case produced significantly different values for the velocity, while the medium and fine meshes produced nearly identical values.

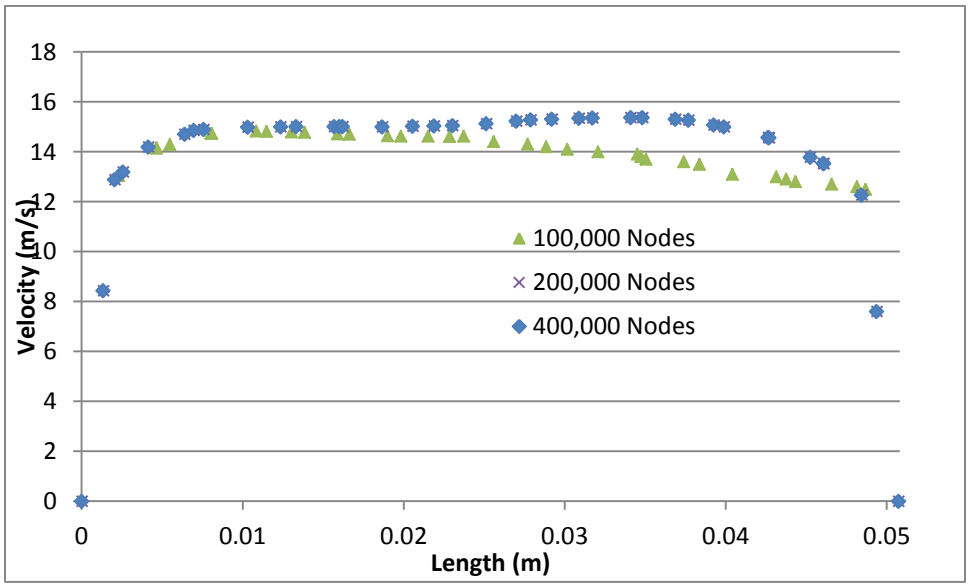

Figure 14: Comparison of Nozzle Velocity for Different Mesh Refinements

Since the medium and fine meshes produced nearly identical results for both the injection system centerline and the nozzle, and the 200,000 node case can be run is significantly less time, it was

selected as the mesh to carry out further simulations involving the particle injections to provide additional validation data.

5.2 Wind Tunnel Grid Independence

As was the case with the injection system, three levels of refinement for the mesh were used, with one exception. Initial simulations using a standard fixed mesh across the entire control volume failed to account for the significant size difference between the velocity inlet and the size of the total control volume. Initial simulations produced velocity profiles with significant error in the initialized velocity condition which is apparent in figure 15.

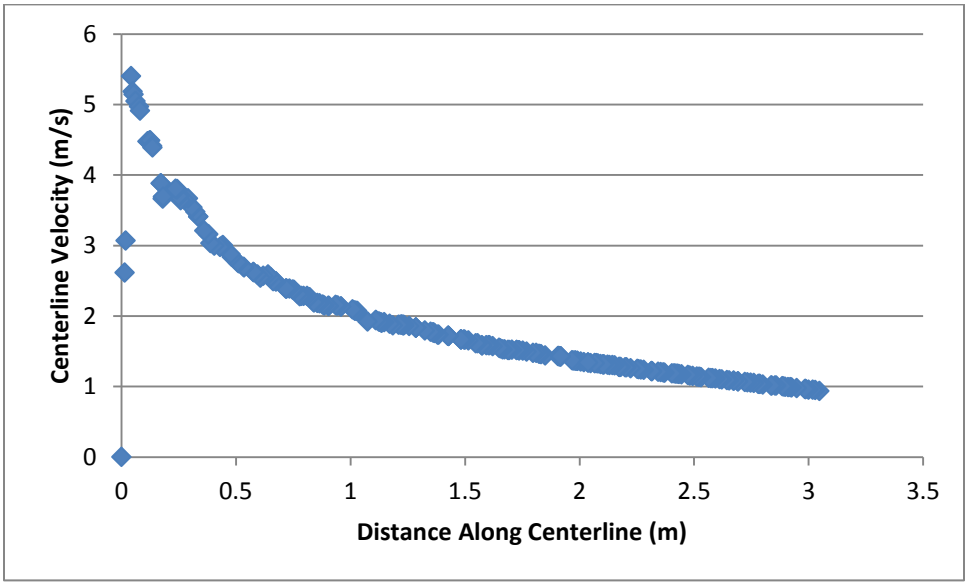

Figure 15: Centerline Velocity of Total Control Volume Fixed Sizing Mesh

The imposed wall condition around the nozzle forces the velocity of the points around the nozzle to zero. This causes significant error if the nozzle does not have a significant number of cells such that the imposed no-slip wall condition only affects a small percentage of the total number of cells. In order to combat this error without an impractical increase in the total number of nodes, an additional sizing function was added at the nozzle. Sizing functions allows a user to control the size or number of nodes present along a surface or edge. In this case a "face sizing" with a fixed maximum cell size of 1mm was used to provide additional nodes near the nozzle. With the added nodes at the nozzle, the no-slip boundary condition only affected a small number of the cells at the nozzle, allowing a more accurate initialized velocity.

The same meshing technique as the injection system was used to create a series of progressively finer meshes for the wind tunnel containing approximately 100,000 nodes, 200,000 nodes, and 400,000 nodes. The centerline velocities for these three cases can be seen in more detail in figure 16.

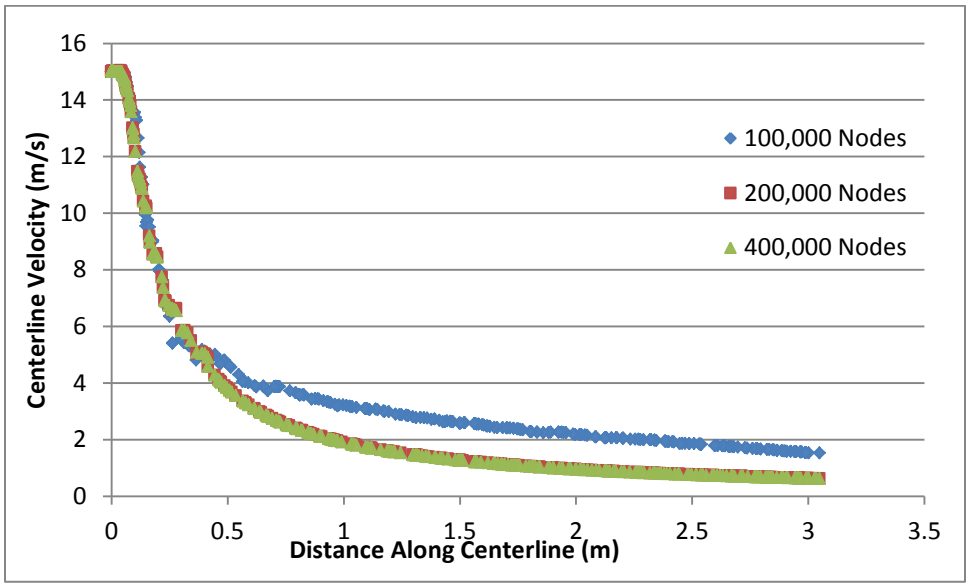

Figure 16: Comparison of Tunnel jet Centerline Velocities for Different Mesh Refinements

The figure shows a significant error for the coarsest mesh tested. In this case, the elements are too large to effectively calculate the dissipation leading to a higher predicted velocity. In addition, due to the large control volume, with a smaller region of high fluctuations, grid adaptations were investigated as a potential solution to create a mesh of sufficient refinement for the jet core. Attempts to produce a mesh of sufficient refinement within the jet core did not appreciably increase the accuracy of the model or decrease the time and computational need. In future simulations, if significantly higher jet velocities are required, FLUENT possesses the ability to refine meshes based on gradients which could be used to produce targeted refinements at points within the shear layer of the jet without increasing the total number of cells to an unreasonable level.

Chapter 6: Injection System Simulation Results

This section details the results of the computational simulation for both the injection system as well as the quiescent environment. The results evaluated include flow field evaluation in relation to a theoretical solution and particle dispersion patterns.

6.1 Injection System Flow Field Results

The first result gathered from the particle injection system was a general flow profile set at the center plane of the geometry. The goal of generating this profile was in part to see the significance of the change in pipe diameter upstream from the actual injection system. As can be seen below in Figure 17, the fluid behaves similar to the jet mechanics present in the larger quiescent environment and quickly disperses into standard pipe flow. This view can also be used to determine the flow development in relation to the pipe length. The velocity vector plot shows fairly constant velocity well before the injection port and continues after the port to the nozzle.

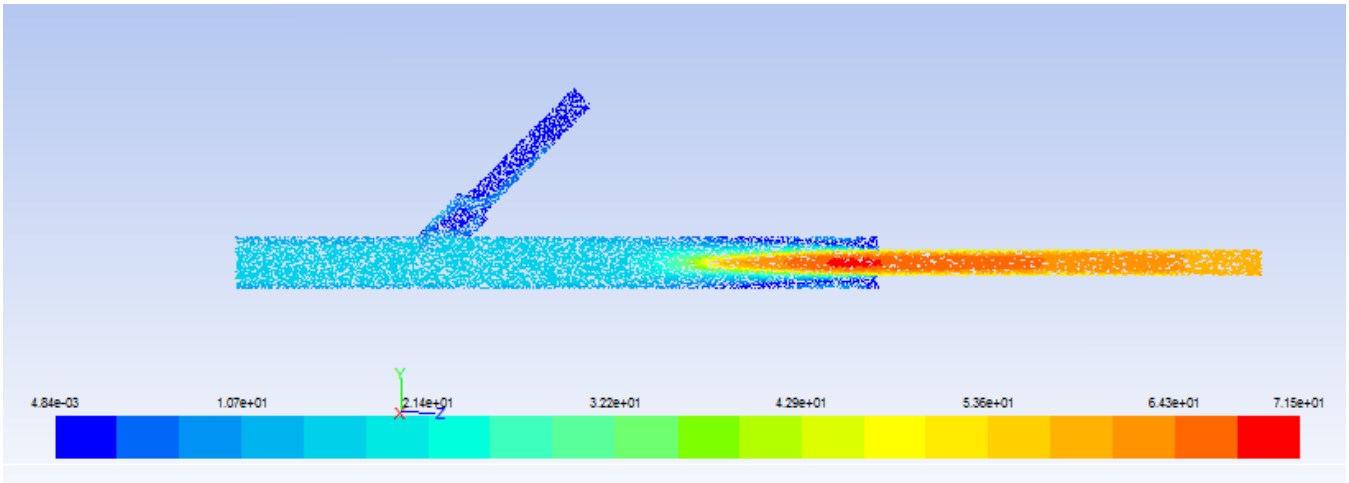

Figure 17: Injection System Center Plane Velocity Profile (m/s)

In order to determine how developed the pipe flow was at the nozzle where it ejects into a quiescent environment, a velocity profile was generated for the nozzle (Figure 18). In this case, 0 m indicates the lowest point in the y direction of the nozzle (the lower left point in Figure 17).

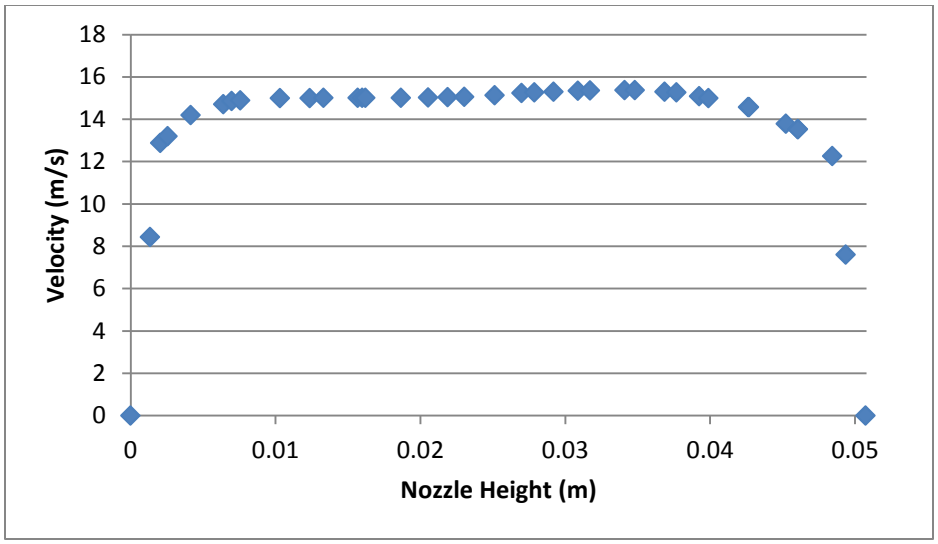

Figure 18: Injection System Nozzle Velocity Where x=0 corresponds to the lowest point along the centerline of the nozzle

The nozzle velocity shows a near constant velocity across the majority of the domain with sharp drops in velocity approaching the walls in keeping with the no slip boundary condition imposed on the walls of the domain. This indicates that the assumption of a constant velocity at the inlet of the quiescent environment was reasonable.

6.2 Injection System Particle Behavior

Since the primary focus of this research is the dispersion and entrainment characteristics of particles in a standard free jet, the effect the particle injection system has on particle behavior leading into the quiescent environment was examined. The first parameter measured was the mean velocity of particles crossing the ejection nozzle. The velocity determined using the Lagrangian tracking scheme can be seen below in Table 3.

Table 3: Particle Injection Velocity at Nozzle

Material Type:	Glass	Glass	Glass	Glass	Chrome Steel	Zirconia-Silica	Zirconia
Measured Mean Particle Diameter (mm):	5.995	3.646	2.602	1.168	2.383	1.121	1.072
Average Nozzle Velocity (m/s)	1.70	1.99	2.25	2.58	1.61	2.77	2.43
Nozzle Velocity Standard Deviation (m/s)	.1070	.0876	.0860	.1376	.1216	.1094	.0938

The simulation of the glass particles showed that particle size played a significant role in the velocity of the particle at the nozzle. As the particle size decreases, the velocity at which the particle leaves the control volume increases due to the added interaction between the particle and the fluid phase. This can be seen in detail by comparing the particle tracking paths displayed below in Figure 19.

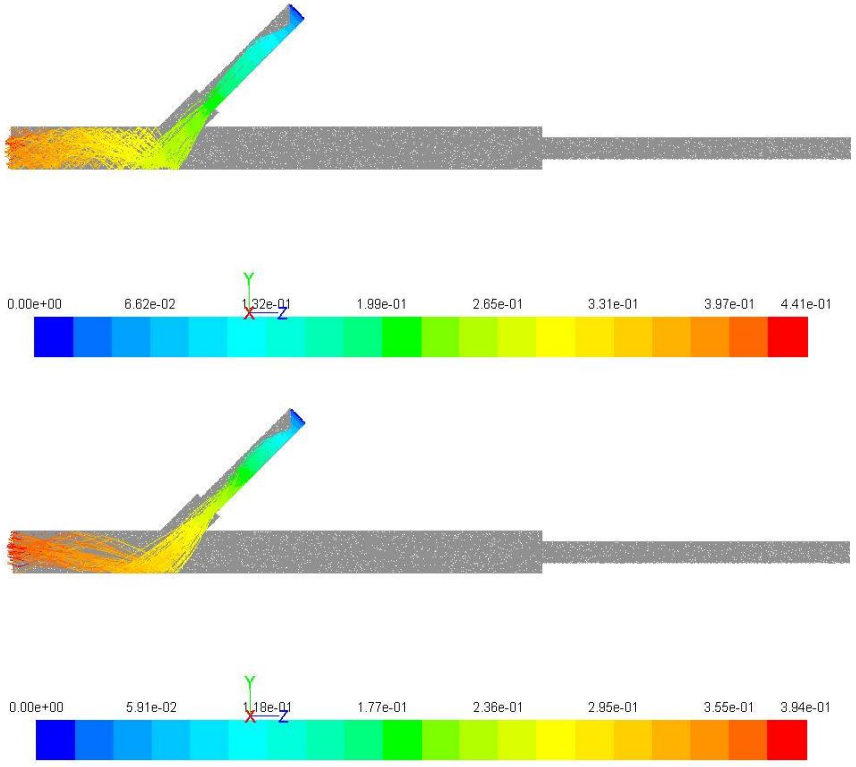

Figure 19: Particle Tracking Displays for 5.99 mm (Top) and 1.168 mm Glass (Bottom) Color Coded by Particle Residence Time

The tracking schemes show two different types of dominant behavior at different points within the domain. When the smaller particles fall from the injection surface, the higher level of interaction with the flow causes the location of the first bounce to become more determinative of the particle location and distribution across the nozzle as the velocity of the particles quickly increases carrying the particle out of the domain. This can be seen by the fact that the majority of the 1.16 mm glass particles bounce once and are then carried out of the domain by the flow. In contrast, while the larger particles do still have bouncing causing some of the behavior, the flow field is insufficiently strong to overcome all of the inertial effects of the particles as it was with the smaller and lighter particles. This creates a particle concentration bias across the nozzle

where the mean starting particle position deviates from the center of the jet. This will be discussed in additional detail in the following section. The intermediate sizes (2.60 mm and 3.64 mm) show behavior with aspects of both the 1.16 mm and 5.99 mm, where the 2.60 mm particles show a similar limited bouncing behavior due to a higher level of interaction with the flow. In this case, however, the particles have sufficient inertia as to change the final location of the particles at the nozzle. The 3.64 mm particles show a very similar behavior to the 5.99 mm case, sharing the more randomly spread particle dispersion.

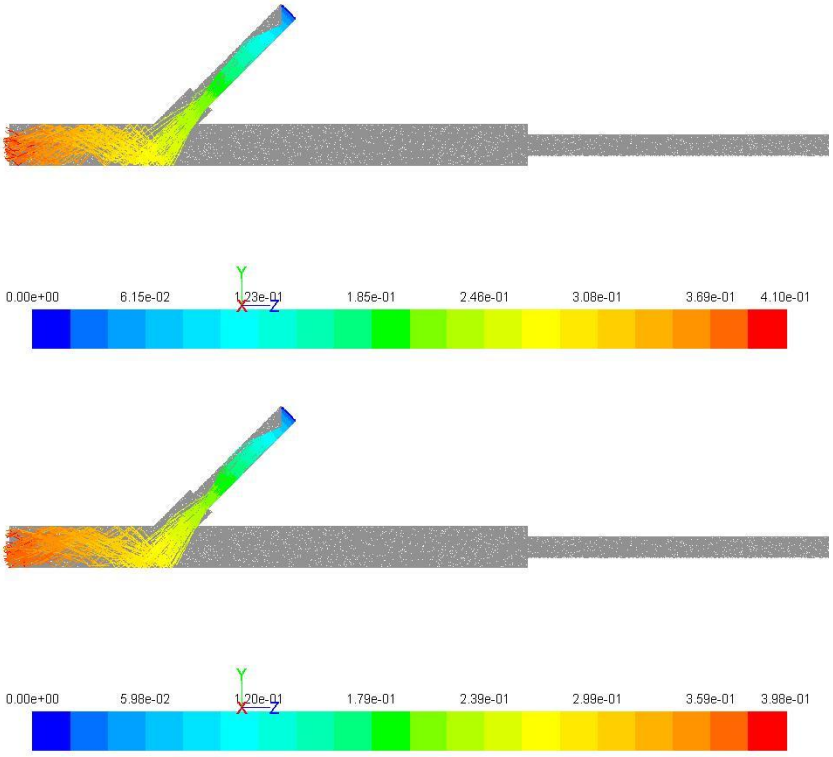

Figure 20: Particle Tracking Displays for 3.64 mm (Top) and 2.60 mm Glass (Bottom) Color Coded by Particle Residence Time

In order to compare the effect density has on the particle dispersion within the injection system, the 1.168 mm glass, 1.121 mm Zirconia Silica, and 1.071 mm Zirconia particle tracks were compared. The particle dispersion tracking paths for the Zirconia-Silica and Zirconia can be seen in Figure 21.

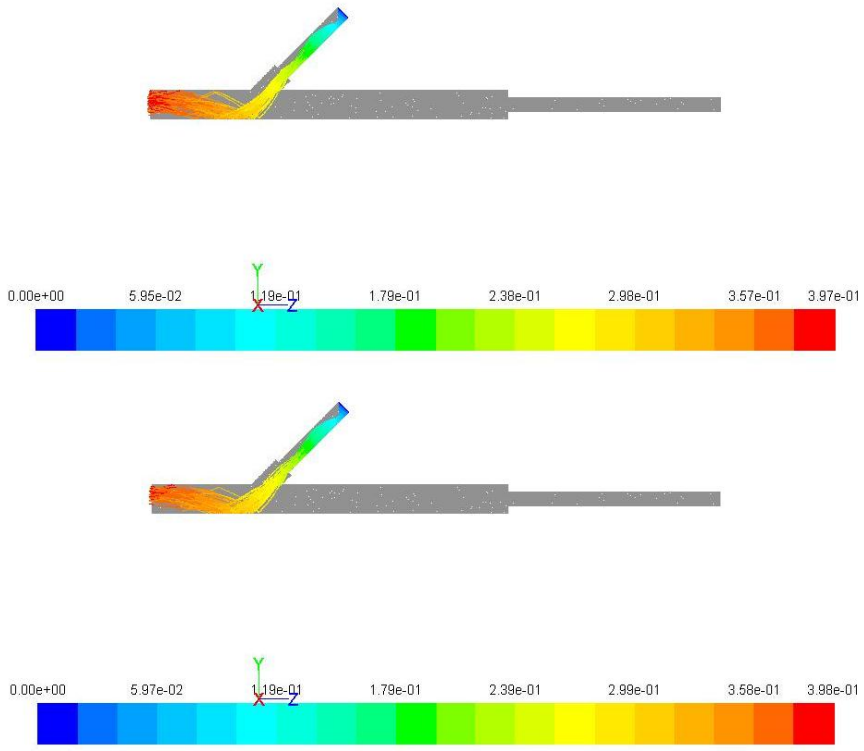

Figure 21: Particle Tracking Displays for 1.071 mm Zirconia (Top) and 1.121 mm Zirconia-Silica (Bottom) Color Coded by Particle Residence Time

The Zirconia-Silica particle which is approximately 50% more dense than glass has similar behavior to the glass. Once the particle exits the injection tube, it falls under the force of gravity until it bounces off the bottom surface and is then entrained in the flow which causes a bias to the top half of the pipe due to the distance of the nozzle from the injection port. In contrast, the 1.071 Zirconia particles bounce more than once within the pipe which causes a greater dispersion across the inlet, however, due to the location of the nozzle there is still a partial bias toward the top half of the nozzle.

For comparison purposes, histograms of the particle location across the nozzle can be seen for each case below. Special attention should be paid to the Glass 1.168 mm and Zirconia-Silica 1.121 mm since they have the highest dispersion bias toward one half of the pipe. In addition, the Zirconia 1.072 mm particles also have a slight bias to the top half of the duct and the Glass 3.646mm has a slight bias to the lower half of the nozzle.

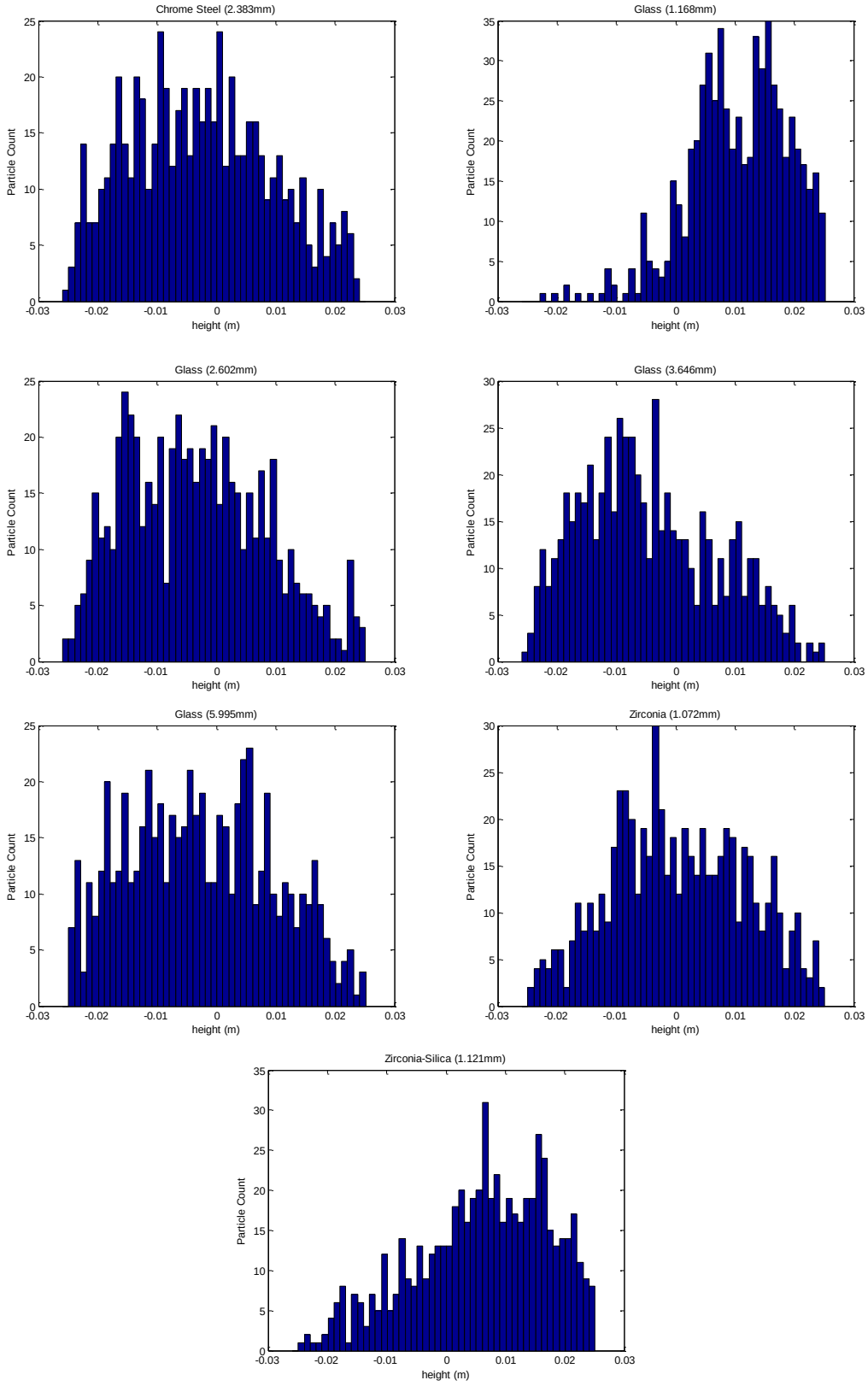

Figure 22: Histograms of Dispersion of Tested Particles Across Nozzle

The results of the particle dispersion do not show a clear generalized relationship between particle size or density and distribution across the nozzle, but instead introduce a potential source of experimental improvement by altering the geometry to lessen the random nature of the distribution across the outlet.

6.3 Modified Particle Injection System

Due to the non-uniform distribution across the nozzle, new geometries were designed in order to provide results for future experimental development. The first geometry tested was identical to the original with an additional 12 inches of pipe added at the nozzle. In addition, a case using the original geometry rotated 180° such that the particles must be given some initial velocity to overcome the effect of gravity to enter the injection system

6.3.1 Extended Pipe Geometry

The first geometry tested used an extended pipe following the injection source as seen in Figure 23.

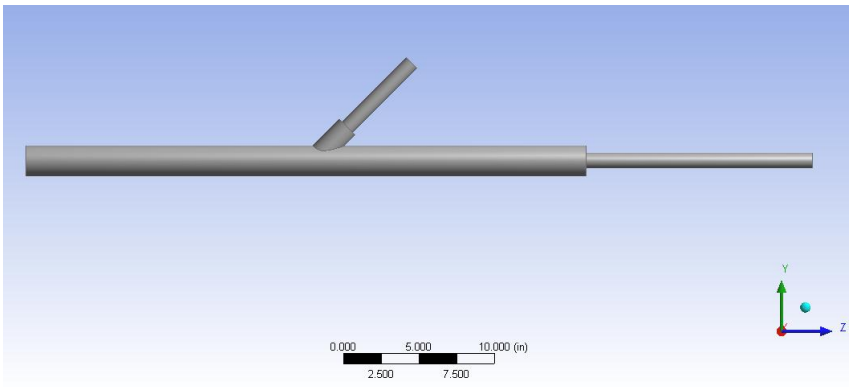

Figure 23: Extended Geometry Test Case

The intention for this geometry was to investigate if the bouncing mechanism, which drastically affects the nozzle dispersion distribution, would have the same effect in a longer length of pipe. The simulation produced a very similar velocity profile as the original geometry, with the exception that the flow is more uniform along the last 20” of the pipe leading to the nozzle. The velocity flow field can be seen in greater detail in Figure 24 and when compared to Figure 17 shows no significant change beyond extending the section of fully developed flow.

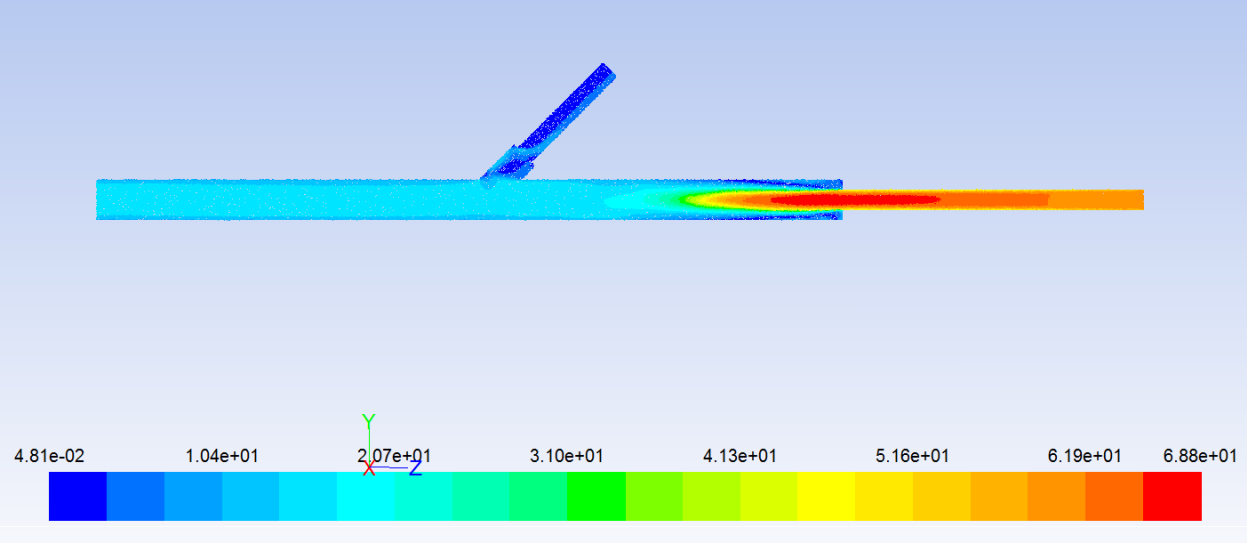

Figure 24: Extended Geometry Velocity Flow Field

The nozzle velocity profile for the extended geometry was compared to the original geometry in order to determine what nozzle effect, if any, the added length would have on the velocity profile that enters the quiescent environment. The profiles for each geometry can be seen in Figure 25. The velocity profile shares the same blunted profile characteristic of fully developed flow which indicates that the added geometry has little to no effect on the flow and instead can be evaluated for a particle dispersion effect.

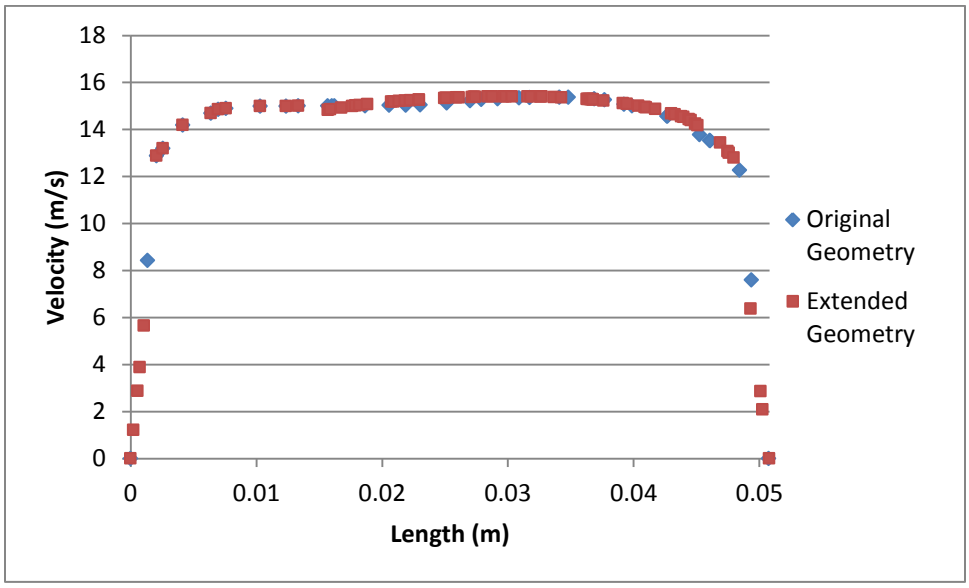

Figure 25: Comparison of Extended Geometry Nozzle Velocity

Once the nozzle velocities for each geometry were compared, the particle tracking for each of the cases tested was simulated using the same Lagrangian tracking scheme. The first comparison for the new geometry was the average particle velocity at the nozzle which can be seen in Table 4.

Table 4: Extended Geometry Particle Velocities

Material Type:	Glass	Glass	Glass	Glass	Chrome Steel	Zirconia-Silica	Zirconia
Measured Mean Particle Diameter (mm):	5.995	3.646	2.602	1.168	2.383	1.121	1.072
Average Nozzle Velocity (m/s)	2.24	3.00	3.11	4.99	2.11	3.88	3.39
Nozzle Velocity Standard Deviation (m/s)	.0945	.119	.099	.113	.093	.1189	.1055
Percent Change from Original (%)	31.7	50.7	38.2	57.4	31.1	40.1	39.5

The particle velocities are consistently higher for the extended pipe length with minor changes for the standard deviation across all particle sizes and materials. The increase in velocity can be attributed to the additional time required for the particles to reach the nozzle. The additional length allows the particles to become more entrained with the flow. This is particularly important for the smaller particles which had a significant increase in velocity. This could complicate experimental procedures if the additional velocity is not accounted for.

In addition, the particle distribution across the nozzle is significantly affected by the increase in pipe length for certain particle sizes and densities. Figure 26 demonstrates that the additional pipe length produces a particle distribution across the nozzle with a significantly more Gaussian distribution for the cases which showed the greatest bias in the standard configuration. The distributions for the new geometry can be seen in detail in Figure 27 as a particle tracking scheme.

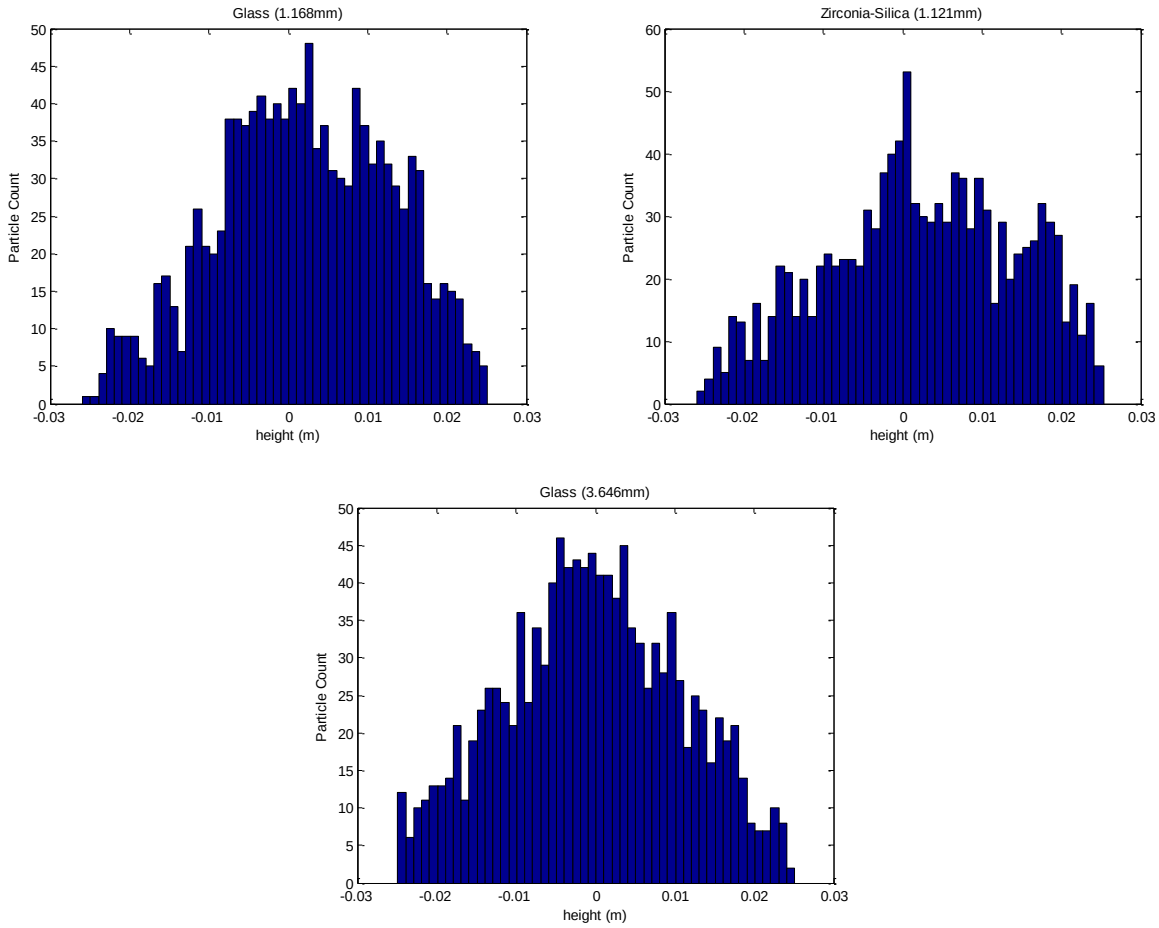

Figure 26: Particle Distribution Across Nozzle

The distribution for all of these cases was shown to be significantly more Gaussian for these particles within the new geometry. The remaining particle sizes and densities showed less significant changes in distribution, however, all cases did tend toward a more Gaussian distribution on the whole. The behavior of the three distributions with the most significant changes is easier to see when comparing the Lagrangian particle history data.

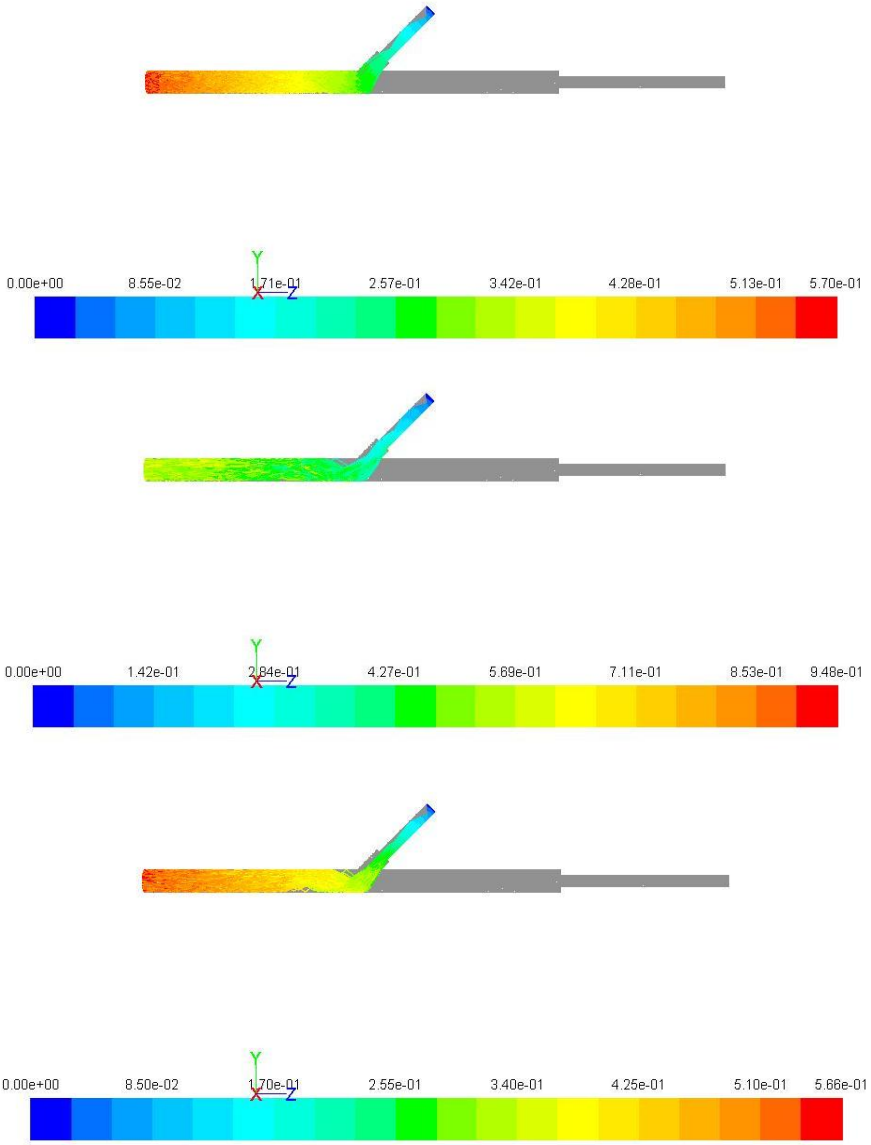

Figure 27: Particle Tracking Displays for 3.646 mm Glass (Top), 1.168 mm Glass (middle), and 1.121 mm Zirconia-Silica (Bottom) Color Coded by Particle Residence Time

The particle tracking plots show the same initial behavior in both geometries, however, due to the additional length added, the particle bouncing plays a less significant role in the distribution. For the particles displayed, the initial bounces occur with similar behavior, but because the nozzle is an additional 12 inches away, additional bounces and entrainment can occur in order better mix the particles within the flow.

Given the improvement in particle distribution, this change in geometry is most likely the simplest alteration to the experimental geometry that could provide more reliable and consistent results for future tests.

6.3.2 Modified Operating Conditions

An additional method to improve the quality of particle distribution in the injection system was to alter the operating condition and orientation of the system as a whole. A common practice in testing particle dispersion is to use acoustic forcing of particles to orient them in a particular structure. That idea inspired a method in an attempt to limit the effect that initial particle bouncing has on the system. In this configuration, the injection system is rotated 180° such that particles must be forced up into the system with some initial velocity to overcome the gravitational force instead of letting gravity pull the particles into the pipe.

This method creates some complications in selecting an initial velocity for the particle injections. For that reason, the simulations provide two functions: determining an initial velocity capable of injecting particles into the flow and determining what effect this method has on the particle distribution across the nozzle. The initial velocities for the particle injections were individually iteratively derived based on an initial estimate for the particles to take the same amount of time to reach the pipe flow using the standard equations of motion. These basic calculations produce a velocity of 2.048 m/s normal to the injection surface (at a 45° angle to the pipe flow). The iteration process produced the following velocity/particle combinations which produced the most normal particle distribution can be seen in Table 5 below.

Table 5: Initial Particle Velocity for Modified Injection System

Material Type:	Glass	Glass	Glass	Glass	Chrome Steel	Zirconia-Silica	Zirconia
Measured Mean Particle Diameter (mm):	5.995	3.646	2.602	1.168	2.383	1.121	1.072
Particle Injection Velocity: Normal to Surface (m/s)	2.26	2.47	2.54	2.54	2.26	2.33	2.68

The particle distribution can be seen for the particles tested below in Figure 28. Compared to the original geometry with gravity fed injection, the distribution using an initial velocity injection follows a significantly more normal distribution across all cases. The particles produced very similar velocities and standard deviations as the original geometry (the values can be seen in Table 6), which indicates that the initial velocity and injection again the force of gravity has a less significant effect on the velocity of particles leaving the nozzle. If the geometry tested cannot be easily altered, simply inverting the injection system and designing a secondary system to inject particles could be a viable method to produce more normal distributions.

Table 6: Particle Nozzle Velocity for Initial Velocity Condition

Material Type:	Glass	Glass	Glass	Glass	Chrome Steel	Zirconia-Silica	Zirconia
Measured Mean Particle Diameter (mm):	5.995	3.646	2.602	1.168	2.383	1.121	1.072
Average Nozzle Velocity (m/s)	1.57	1.95	2.21	3.07	1.48	2.64	2.43
Nozzle Velocity Standard Deviation (m/s)	.118	.125	.125	.161	.118	.159	.136

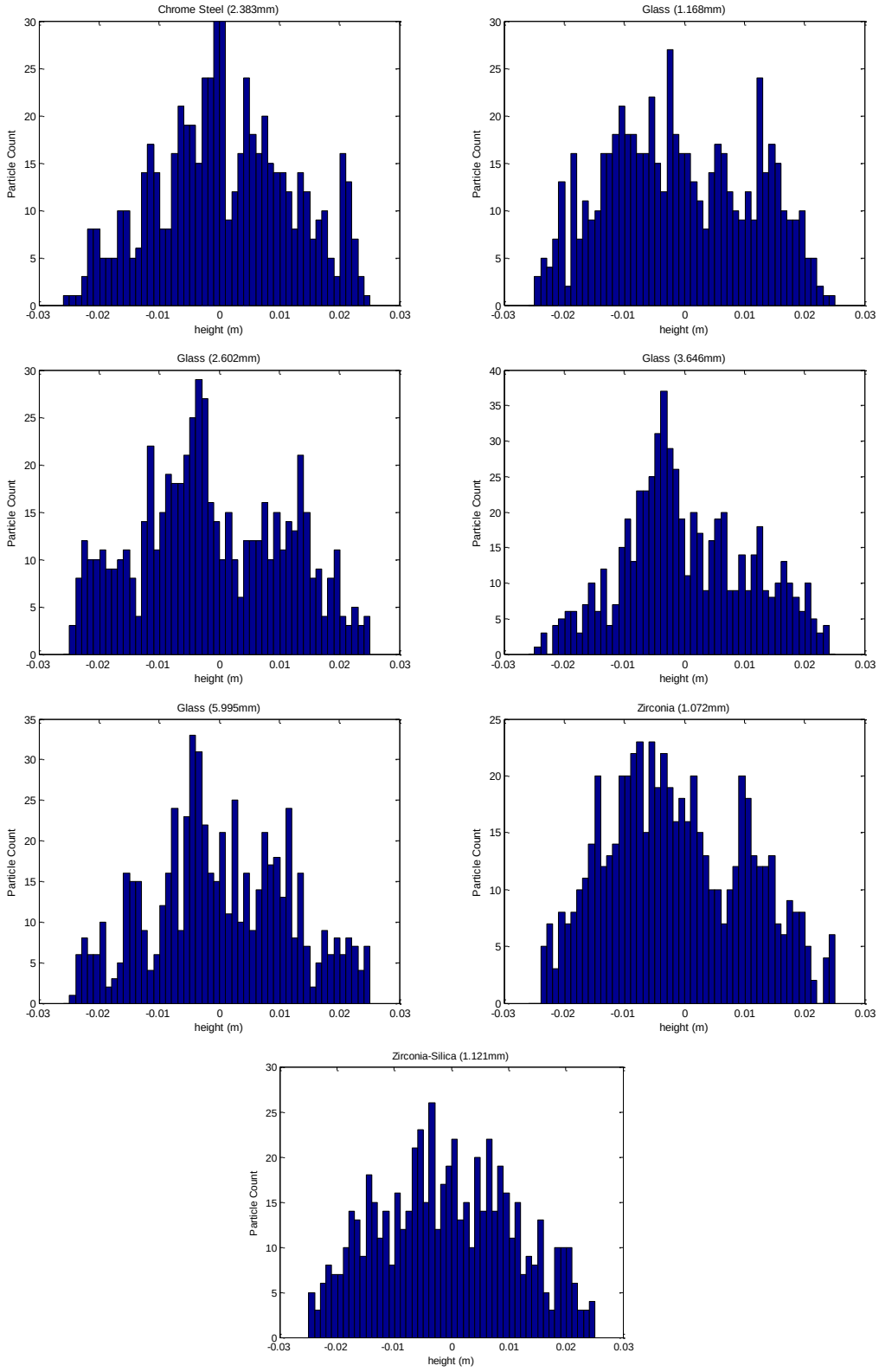

Figure 28: Histograms of Dispersion of Tested Particles Across Nozzle Using Modified Operating Conditions

Due to the limitations in collecting experimental data, the results of this simulation were used to perform additional tests on the wind tunnel side of the simulation. The simulation results which produced some non-zero velocities for particle exiting the injection system were used to better predict the behavior of injected particles compared to stationary particle injections directly at the nozzle of the system. In addition, the simulation which illustrated a heavily non-uniform particle distribution across the nozzle was used to create secondary simulations which would test the effect of discretizing the nozzle into regions where the effect of starting height in the nozzle could be measured relative to particle dispersion.

Chapter 7: Wind Tunnel Results

Initial experimental results as well as results from the simulation of the injection system revealed the need to test two configurations of the wind tunnel for simulation. The experimental results indicated a non-symmetric distribution of particles falling out of entrainment within the jet core. It was speculated that this was due to an uneven particle distribution at the nozzle exit. For this reason, a different inlet was created where the particle distribution could be weight to either the top or bottom half of the nozzle and was tested along with the standard uniform distribution.

7.1 Simulation Flow Field Evaluation

The results of the simulation were first analyzed in relation to the flow field, and how close it matched a theoretical case for an axisymmetric turbulent jet. This was accomplished by comparing the centerline velocity of the simulation to a theoretical one using equation (1) where B_u was taken to be 5.0. In this case, the simulation used a nozzle velocity of 14.29 m/s (the average velocity of the fully developed flow measured using a Pitot tube anemometer). The comparison of the centerline velocities can be seen in Figure 29 below. The defining difference between the two cases is the slight over-estimation of the velocity at the beginning of the jet core. This difference is less significant at points down stream.

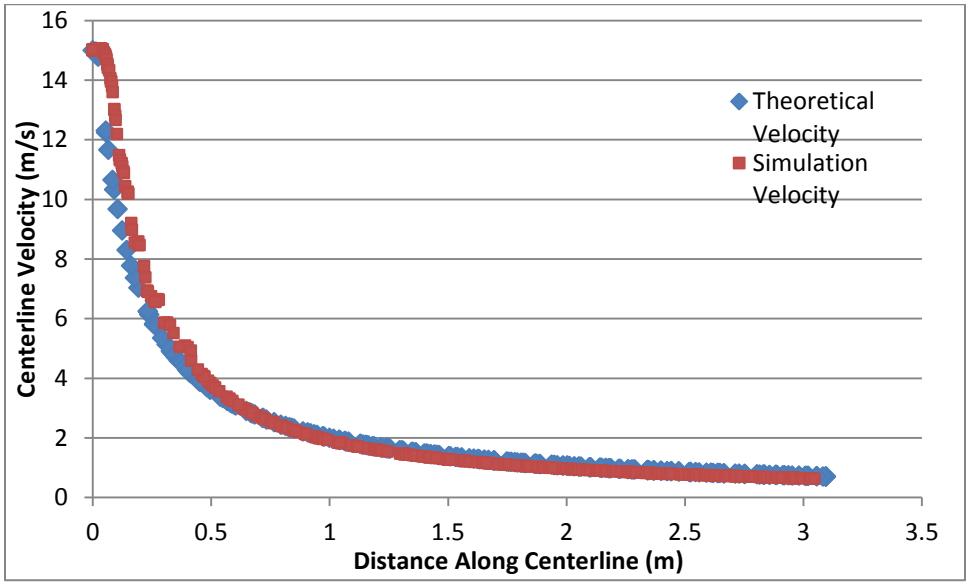

Figure 29: Comparison of Theoretical and Simulated Jet Centerline Velocity

In addition to the centerline velocity comparison, the spreading angle of the jet simulation was compared to experimental and theoretical studies on turbulent axisymmetric jets. As was shown previously, the simulated spreading rate of the jet was approximately 12°, fitting well with the

theoretical result of 11.8°. Due to this agreement between the simulated and theoretical results, the simulation was used to test particle dispersion for the cases mentioned in Chapter 6.

7.2 Particle Dispersion Patterns

The particle dispersion simulation was broken down into a variety of different cases in order to test which aspects of the dispersion were a result of conditions unique to the experimental apparatus. The first case was deemed a "static injection" where the particles would be injected with zero initial velocity across the nozzle. This condition would be difficult to replicate experimentally given the current set up. The second condition better reflected the experimental results, wherein the particles were given initial velocities equal to the mean velocity calculated from the simulation of the injection system.

The Stokes number for each case studied was calculated using equation (21) using the characteristic velocity of the jet. The particles tested provide a wide range of values and can be seen in Table 7.

Table 7: Calculated Stokes Numbers for Particles Tested Within the Jet Geometry

Material Type:	Glass	Glass	Glass	Glass	Chrome Steel	Zirconia-Silica	Zirconia
Measured Mean Particle Diameter (mm):	5.995	3.646	2.602	1.168	2.383	1.121	1.072
Particle Stokes Number	251.71	93.09	47.42	9.55	125.72	13.02	17.71

While all of the cases studied are outside the Standard Stokes regime (St≈1), it is expected that the particles will not act explicitly as tracers to the flow. However, the 1mm scale particles could show signs of Stokes flow and show higher adherence to flow path lines with substantial lag time.

In addition to the Stokes number for each particle case, the Kolmogorov scale was calculated to provide another method of quantifying the interaction between the fluid flow and the particle motion. Compared to the box experiment discussed in Chapter 4, the inlet velocity of this case is significantly lower, which will cause the Kolmogorov scale to be smaller. For this case, the turbulent kinetic energy dissipation rate (ε) was taken from the results of the flow simulation,

and was spatially averaged to be 50 m^2/s^3. By using this value with equation 22, the Kolmogorov scale was calculated to be 90 microns (.09 mm). Given that all particles sizes tested are at least one order of magnitude greater than the Kolmogorov scale, long term entrainment would not be expected for any case.

A sample particle tracking result for these two conditions can be seen in Figure 30 below. The particle injections show drastic differences in both the magnitude of distance traveled by the particles, as well as the distribution across the domain. The static injection shows a minimal displacement for the particles, with a high level of dispersion. The dynamic injection shows the opposite characteristics with a much higher displacement and a more compact distribution of particles. This result is related in part to the low velocity of the fluid exiting the nozzle. In the case of the static injection, the particles injected in the lower extreme of the nozzle tend to simply fall with minimal change in velocity. For particles experiencing the higher velocities at the center of the jet core, the displacement is more significant. By comparison, in the dynamic injection, the particles already have sufficient forward momentum that the flow does not need to transfer as much energy to cause significant displacements. This behavior was seen across all particle sizes and materials, while the 1mm scale particles showed the largest difference in displacement.

a)

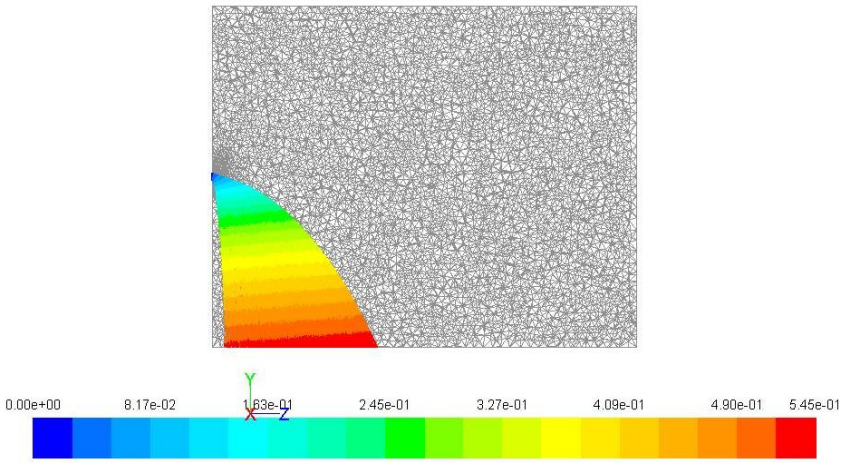

b)

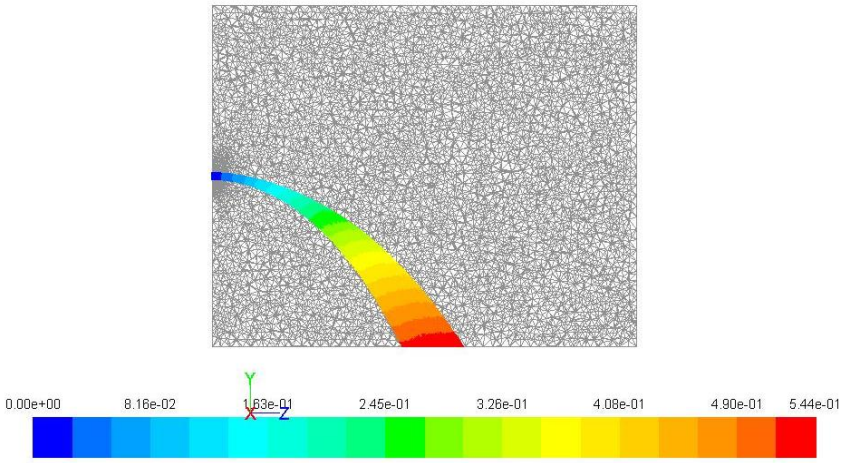

Figure 30: a) Particle Tracking Result for 1.168mm Glass Static Particle Injection Color Coded by Particle Residence Time (s) b) Particle Tracking Result for 1.168mm Glass Initial Velocity Particle Injection Color Coded by Particle Residence Time (s)

A variety of particle dispersion characteristics were compared between the simulation of the dynamic particle injection and the experimental results. The first and simplest parameter tested was average distance traveled into the quiescent environment for the various particle injections. Table 8 shows that the simulation effectively predicted the displacement of the particles within 2 to 12% of the experimental results depending on the particle tested. The simulation produced the least accurate results for the 1mm scale glass and zirconia-silica particles, with errors of 9.476% and 11.568% respectively compared to the experimental results. This significant increase in error is due to the result generated through simulation of the injection system where it was shown

that for the 1mm scale glass and zirconia-silica there was a significant distribution bias toward the top half of the nozzle. More detail on this issue will be discussed in section 7.3. Beyond these two cases, there is minimal information to develop a trend for the error between the simulation and experimentation.

Table 8: Comparison of Experimental and Simulation Mean Particle Displacement

Material Type:	Glass	Glass	Glass	Glass	Chrome Steel	Zirconia-Silica	Zirconia
Measured Mean Particle Diameter (mm):	5.995	3.646	2.602	1.168	2.383	1.121	1.072
Experimental Displacement (in)	29.7	37.465	43.527	63.724	23.784	53.776	44.451
Simulated Displacement(m/s)	28.061	39.219	42.164	58.208	22.262	48.200	43.186
Percent Difference (%)	5.841	4.682	3.232	9.476	6.837	11.568	2.929

In comparison, the standard deviation of the simulated particle displacement was higher for the majority of the cases tested. A comparison of the standard deviations for each particle type can be seen in Table 9 below. The only particle which had a smaller standard deviation was 1.168mm glass, while the 1.121mm Zirconia-Silica had the closest approximation. Previous simulations designed to test the particle distribution across the nozzle of the injection system presented a possible solution for the discrepancy between the two cases. Simulations of the injection system illustrated there was a non-uniform distribution of particles across the nozzle, while this simulation was carried out with a uniform distribution across the nozzle for all cases. While this was done as an initial test of the accuracy of the simulation, it could provide some

error as it does not match the experimental set up as effectively as it could since particle experience different forces dependent on their location within the jet core.

Table 9: Comparison of Experimental and Simulation Particle Displacement Standard Deviation

Material Type:	Glass	Glass	Glass	Glass	Chrome Steel	Zirconia-Silica	Zirconia
Measured Mean Particle Diameter (mm):	5.995	3.646	2.602	1.168	2.383	1.121	1.072
Experimental Standard Deviation(in)	6.444	7.313	5.314	12.800	5.314	10.794	9.852
Simulated Standard Deviation(in)	16.863	10.121	6.123	8.984	7.582	10.943	12.806
Percent Difference (%)	61.785	27.744	13.209	42.477	29.915	1.365	23.065

For comparison purposes, the histograms generated from the experimental data and the uniform nozzle distribution can be found in Appendix A. In order test the relationship between nozzle position at the injection and displacement within the jet, Figure 31 was generated to compare these two parameters.

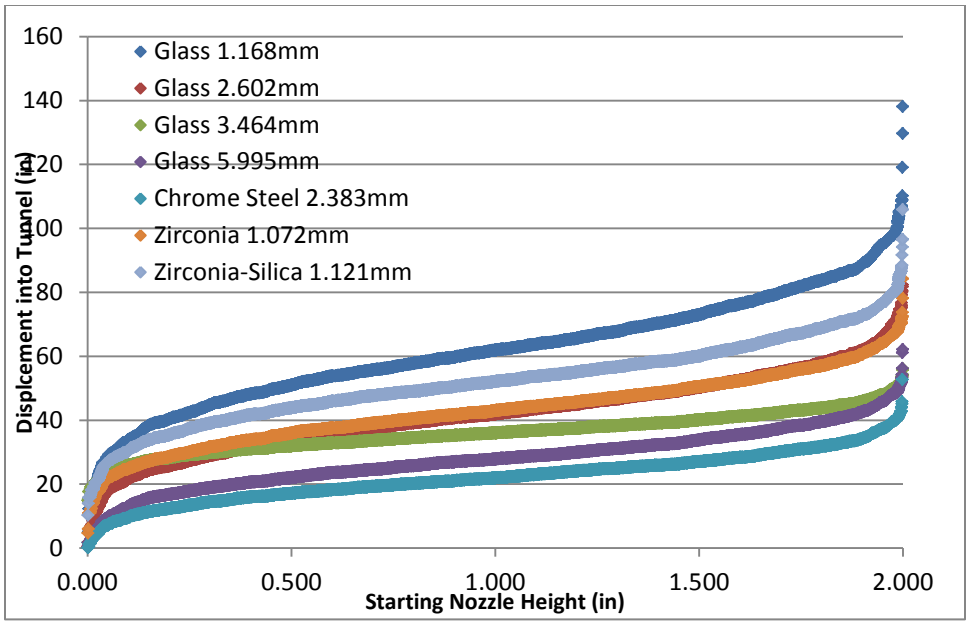

Figure 31: Comparison of Initial Nozzle Height to Normal Displacement

The relationship between particle starting height and displacement occurred as expected with the most significant displacement changes occurring for particles at the highest and lowest positions within the nozzle. This result is due to a combination of jet structures and Newtonian mechanics. The most obvious reason is that particles at the bottom of the nozzle are closer to the ground, and in the absence of significant vertical velocity gradients in the flow, would impact first independent of the horizontal velocity. This is, however, an over simplification of the system as it ignores the actual jet dynamics. Velocity gradients acting in the vertical direction are in fact present, and these gradients can affect the trajectory of particles. To demonstrate this velocity gradient, a series of plots were generated showing the vertical velocity component of the flow across the jet core with a fixed x distance across the tunnel and at a series of fixed z distances into the tunnel.

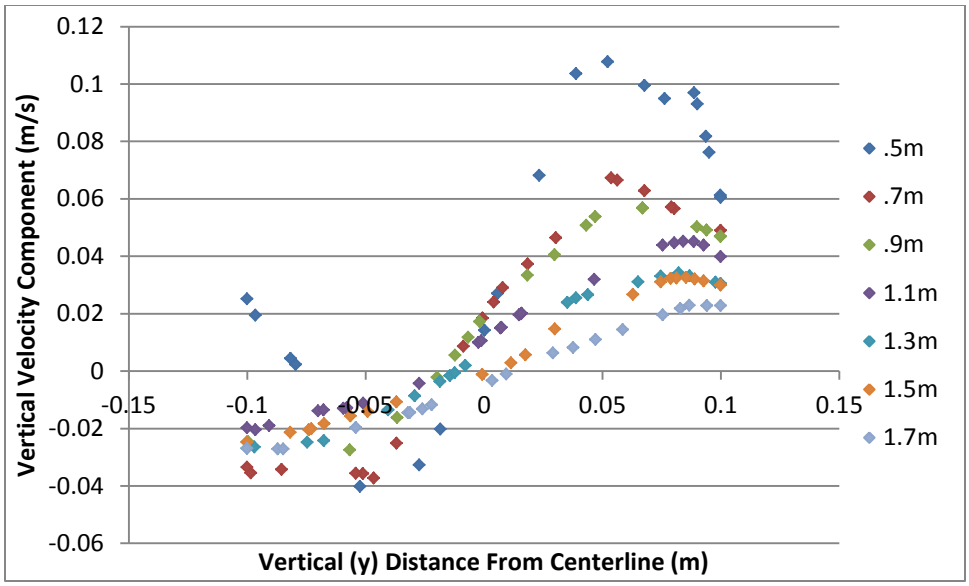

Figure 32: Comparison of Vertical Velocity Component at Various Positions along the Jet Core

This plot shows the steady vertical velocity component and the fact that the transition from negative to positive occurs around the centerline of the nozzle. For this reason, particles injected on the top half of the nozzle are exposed to an additional lift component present in the flow field caused by the entrainment of ambient air. This effect is especially important as the Stokes number decreases in the system. As was previously stated, the Stokes number can be used to measure how closely a particle will follow the flow path lines it is exposed to. Since Stokes number is affected by particle size and particle density, it would be expected to see the 1mm scale particles be the most affected by the velocity gradients in the flow. This result is seen in both the experimental and simulated results for the 1mm scale glass and zirconia-silica, with a lesser effect seen on the 2.602mm Glass and 1.072mm Zirconia, due in part to the higher density of the Zirconia and larger diameter for the glass.

7.3 Particle Dispersion with Nozzle Bias

Experimental results indicated that in most cases, the particle distribution for some cases produced a distribution with a non-zero Skewness, indicating that there is a larger tail on one side of the distribution. The values of the Skewness calculated for the experimental trials can be seen below in Table 10, along with those calculated from the simulated values.

Table 10: Comparison of Skewness from Experimental and Simulated Results

Material Type:	Glass	Glass	Glass	Glass	Chrome Steel	Zirconia-Silica	Zirconia
Measured Mean Particle Diameter (mm):	5.995	3.646	2.602	1.168	2.383	1.121	1.072
Experimental Skewness	0.669	0.619	0.743	-0.788	0.918	0.442	0.540
Simulated Skewness	0.033	0.005	0.065	0.100	0.001	0.043	-0.002

The comparison of the experimental versus simulated condition shows that the simulation produced results that are significantly more Gaussian compared to the experiment. This is due in part to the assumptions made when creating the simulation. For comparison purposes, the histograms for both sets of data can be found in Appendix A. The primary difference is in the particle injection distribution, where the simulation used a uniform distribution across the nozzle. This was shown to be a faulty assumption based on both inspections during experimentation and simulations of the injection system. The simulation of the injection system showed that in each case, there was a bias to one half of the nozzle height. It is important to note that there could also be a bias to the left or right half of the nozzle, but lack of experimental results for comparison led to it not being evaluated.

In an attempt to better match the experimental results, a new simulated geometry was created with the nozzle split into two equal area inlets representing the top and bottom halves of the nozzle. When creating particle injections, this allowed use of the random walk model to produce additional particle tracks across the top or bottom surface in order to create distributions which better matched the results from the simulation of the injection system. Simulations of the injection system showed the greatest disparity in distribution into the tunnel for the 1mm scale glass and Zirconia-Silica and a lesser disparity for the case of the 3.646mm glass. Since these three particle cases showed the most significant nozzle bias and overall high error in the predicted displacement of the particles, they were the initial test cases to determine the effect of the new weighting. The first case evaluated was the 1.168mm glass which showed the highest

nozzle bias with a large majority of particles (~90%) entering the tunnel from the top half of the nozzle. The bias factor used was initially estimated from the results of the injection system simulation, and then changed incrementally until the most accurate results were produced. The bias factor for this case is defined as the percentage of the total number of injected particles traveling through one half of the nozzle. The bias factors that were used for these cases were 90% (top half), 70% (top half), and 67% (bottom half) for the 1.168mm glass, 1.121mm Zirconia-Silica, and 3.646mm glass respectively. This produced a new set of distributions which can be seen in greater detail in Figure 33:

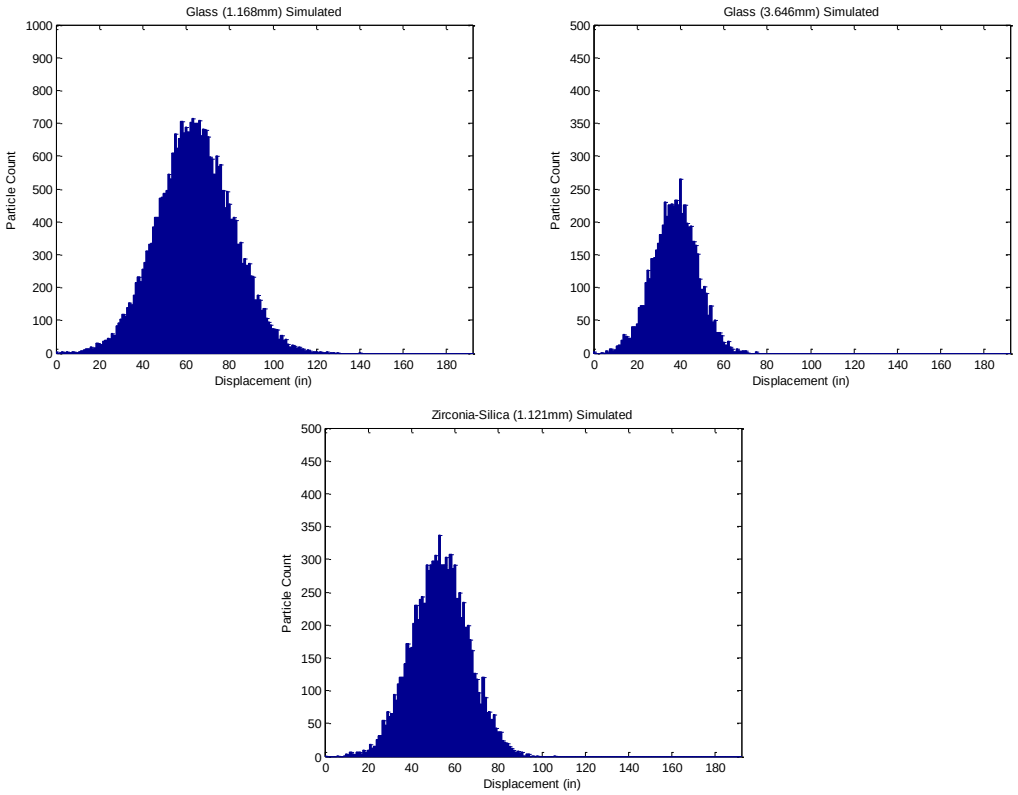

Figure 33: Distributions for Nozzle Bias Cases of Glass 1.168mm, Glass 3.646mm, and Zirconia-Silica 1.121mm

As was the case with the uniform distribution of particles into the tunnel, the particle distribution follows a standard Gaussian profile with an augmented mean from the original case. For the biases used, the new mean more closely matches the experimental results presented in Table 11.

Table 11: Comparison of Experimental and Simulation Mean Particle Displacement Using Nozzle Bias

Material Type:	Glass	Glass	Zirconia-Silica
Measured Mean Particle Diameter (mm):	3.646	1.168	1.121
Experimental Displacement (in)	37.465	63.724	53.776
Simulated Displacement(m/s)	37.514	64.049	53.080
Percent Difference (%)	1.301	0.510	1.311

The added bias factor in the particle count significantly improved the simulated displacement for these three cases, making them the closest matches to the experimental results. This indicates that the model is most effective at simulating the dispersion of particles with a smaller Stokes number compared to predicting the trajectories of larger and or heavier particles. This is partially related to the particles with a higher Stokes number following a more standard rectilinear motion trajectory, with minimal interaction with the flow. For that reason, the particle displacement and distribution would be more significantly affected by the initial position and velocity of the particles upon entering the control volume, propagating any discrepancies in the injection system simulation into the wind tunnel simulation.

Chapter 8: Discussion and Conclusions

It is clear from both the experimental and simulated results that both particle density and size have significant impacts on entrainment properties within turbulent structures. By comparing the cases of the constant density/variable size (glass) case and the constant size/variable density (glass, Zirconia-Silica, Zirconia) it can be easily seen that particle entrainment is dependent on both properties as expected. With the constant density case, the glass particles showed a significantly non-linear relation to displacement for both the experimental and simulated results. This is reasonable as this change affects multiple characteristic forces acting on the particles including gravity, drag, and lift as well as the nature of the particle's interaction with the flow field. In addition, figure 34 shows that the experimental and simulated displacement for the particle have the closest match to a particle undergoing standard ballistic motion as the diameter of the particle increases.

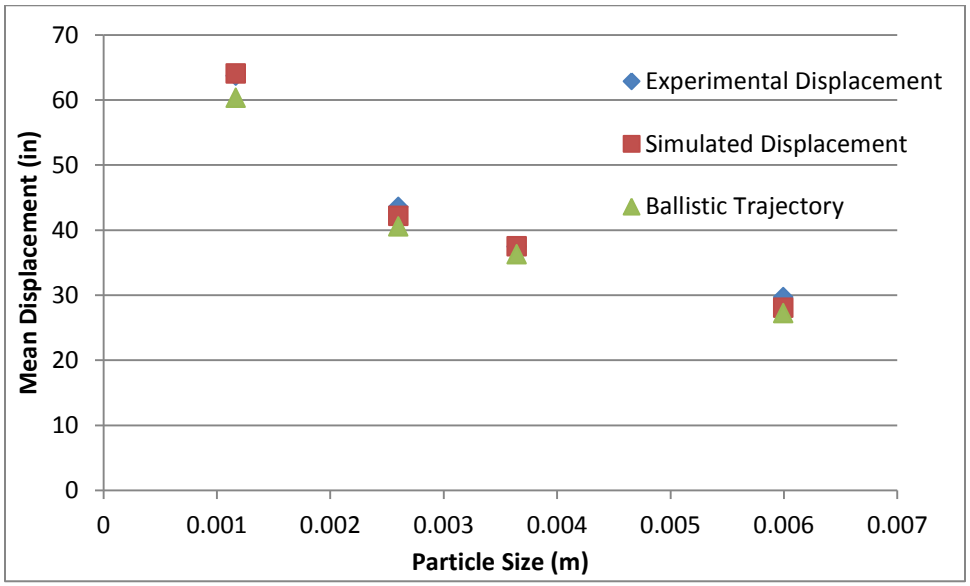

Figure 34: Comparison of Particle Size to Mean Particle Displacement for Various Sizes of Fixed Density (1060 kg/m^3) Glass Particles

In addition to comparing the constant density case, the 1mm scale particles with variable densities were also plotted to show the relationship between particle mass and displacement. The outcome was again as expected, showing that particles with higher mass would fall faster within the system as their inertia would mean interaction with the flow would not significantly alter their trajectory for particles with very high masses. This was especially the case with the

chrome steel particles (experimental value is only 2.1% greater than ballistic displacement). Even though the particles were relatively small in size (2.383 mm) the high density caused the particles to follow a more standard ballistic trajectory out of the nozzle.

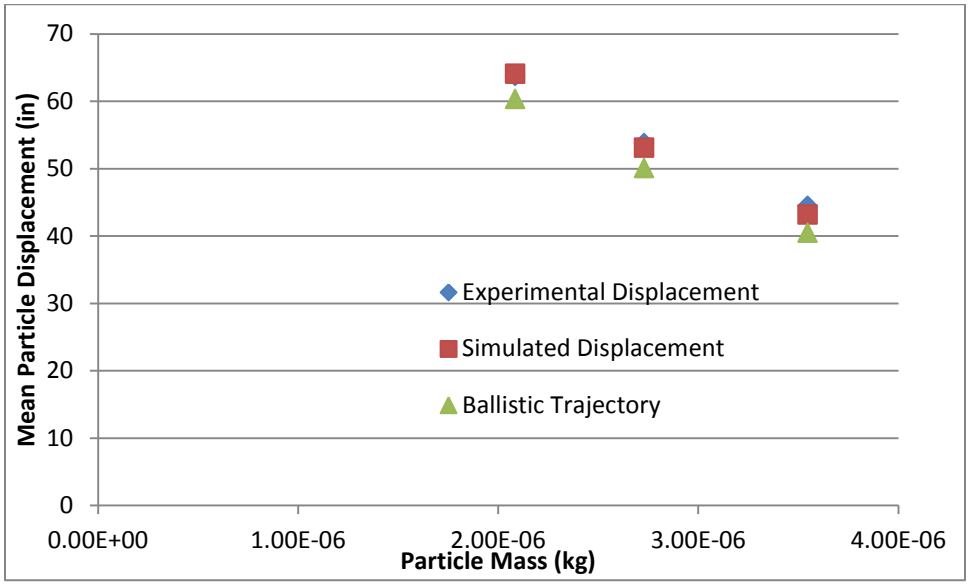

Figure 35: Comparison of Particle Displacement for Particles of Constant Size (1mm) and Variable Density/Mass

Within the turbulent jet, the particle dispersion pattern across the lower surface of the quiescent environment followed a Gaussian distribution for all particle cases tested independent of any nozzle bias used. When comparing the particle displacement as a function of the starting nozzle position, it was seen that the displacement in line with the jet was more significant for particles away from the centerline as seen in Figure 31, where the lighter and smaller particles were the most significantly affected by starting nozzle position. The behavior of particles at the extreme top and bottom of the nozzle at the injection are interesting in that they are exposed to different flow characteristics. Particles at the top of the nozzle would be expected to have the greatest displacement by virtue of the fact that, with constant flow velocity gradients, they would be in the air longer. However, this is only part of the issue. As was shown in Figure 32, the top half of the jet core contains a vertical velocity component compared to the lower half of the core which contains a downward velocity component. It must be noted that for this experiment and simulation, the particle distribution showed significant dependence on the initial velocity and position of the particles injected into the jet core.

In conclusion, the particle dispersion from a turbulent, axisymmetric round jet is predicted to follow a standard Gaussian distribution following their falling out of entrainment within the jet core. The model presented here has a significantly better ability to match particle displacement behavior for cases in which the Stokes number of the system is lower (however in this case is still considered non-Stokesian) as this case produced particle trajectories which better mimic the flow characteristics. When comparing the simulated distributions to the experimental distributions, the clear difference is in the Skewness criteria where the experimental cases show clear non-zero Skewness for several of the particle cases tested. It is speculated that there are conditions present in the experiment that are not accounted for within the model presented. The first experimental difference is in the assumption of a stationary turbulent flow from the experimental set-up. Measurements showed small deviations in the mean flow velocity at the nozzle, which could not be accurately modeled without the addition of more accurate measurement equipment. Since this error could propagate within both the injection system and the wind tunnel, it could produce significant differences in the final particle distributions. In addition, the method of initial particle injection was modeled as simple falling which deviates from the actual operating condition where particles are released through a ball valve.

Chapter 9: Future Work

Additional research based on this project can be divided into two categories: additional simulations to improve the scope of data collected and additional experimentation to validate current models.

9.1 Additional Simulations

While current simulations have produced viable results for comparison to experimentation, the results were shown to be highly dependent on the initial condition imposed upon the particle injections. Future simulations would ideally focus on determining entrainment characteristics based on static injections. This would require one of two changes to the current simulation parameters: either a significant increase in the jet velocity or a significant decrease in the size/density of particles tested or a combination thereof.

Each of these changes would create additional difficulties from a simulation perspective. Increases in the jet velocity would require significant refinement in the mesh used in order to effectively capture the turbulent characteristics. While the mesh refinement is well within the capabilities of FLUENT, the computational power required to run the current simulation configuration at the finest mesh (~400,000 nodes) put a significant strain on the system available. For this reason, additional studies would require additional computing assets in order to run a comprehensive assessment. On the other side of the issue is expanding the range of particle sizes tested. While the particle sizes (and therefore Stokes number) range from well outside the Stokes regime to bordering it (1.16mm glass), additional particles sizes would likely cross the scale into Stokes flow. While this is not a problem, the effect of different forces may no longer be effectively assumed to be zero, as was the case with forces like the Brownian force for the current simulation.

In addition, a model was generated in an attempt to simulate the entire geometry tested (a combined geometry with the injection system directly connected to the wind tunnel), but limitations prevented the simulation from being effectively run. The geometry can be seen in detail in Figure 36.

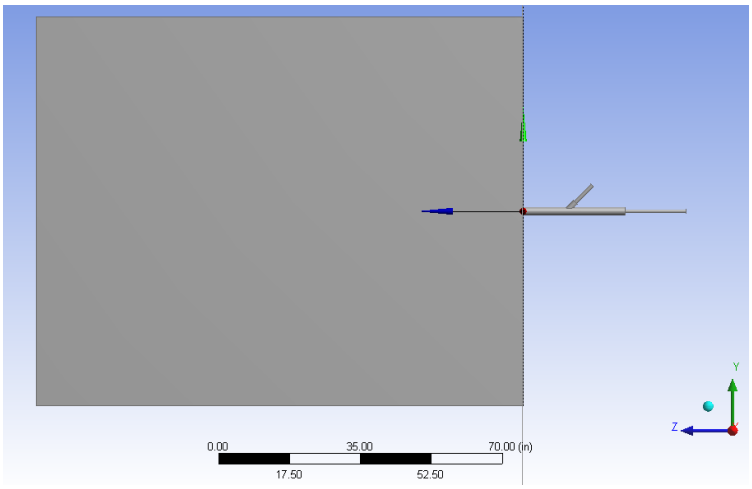

Figure 36: Combined System Geometry

The grid independence study performed for the individual cases (chapter 5) indicated that if the same level of mesh refinement was utilized for the combined geometry, the time required to run any one configuration would be considerable and would likely prohibit the running of multiple cases especially if phase coupling were required based on new volume fractions.

9.2 Experimental Expansion

The primary future experimental work explores validation of the injection system model generated. While some of the aspects of the simulation can at least be speculated, such as the velocity profile uniformity at the nozzle, the simulation results related to particle dispersion could have drastic effects on the accuracy of future models. The experimental results of greatest interest are the same as those collected from the simulation: the particle dispersion across the nozzle and the velocity of particles exiting the injection system. This would require, at minimum, a rebuild of some components of the system to allow visual inspection of the particle behavior within the pipe (i.e. use of transparent piping for the final section). This could be done for any of the configurations simulated here: the original geometry, the extended pipe, or the modified operating condition case. The case which presents the shortest lead time between construction and implementation coupled with the most viability would be the extended pipe. An additional modification to improve the accuracy of results would be to add a particle forcing system in order to control the orientation of the particles entering the control volume. A common method is acoustic forcing in which controlled vibrations are used to transport particles in a more controlled fashion, which could be used to inject particles with more determined trajectories within the injection system. While the current research presented provides a useful

look at dispersion characteristics of particles of varying sizes and properties within turbulent structures, additional considerations would allow for more generalized solutions with a higher level of future repeatability.

Work Cited:

[1] L. Z. Robertson, "Deposition of Newtonian Particles Entrained in a Turbulent Axisymmetric Free Jet," M.S., Mechanical Engineering, Virginia Polytechnic Institute and State University, 2012.

[2] S. N. Laboratories, "PROACT: Bolstering airport defense against chemical or biological attacks," ed, 2004.

[3] G. S. Settles, "Fluid Mechanics and Homeland Security," *Annual Review of Fluid Mechanics,* vol. 38, pp. 87-110, 2006.

[4] M. E. Coleman, B. Thran, S. S. Morse, M. Hugh-Jones, and S. Massulik, "INHALATION ANTHRAX: DOSE RESPONSE AND RISK ANALYSIS," *Biosecurity and Bioterrorism: Biodefense Strategy, Practice, and Science,* vol. 6, 2008.

[5] D. O. Fleming and D. L. Hunt, *Biological Safety - Principles and Practices (4th Edition)*: American Society for Microbiology, 2006.

[6] H. A. Druetta, D. W. Hendersona, L. Packmana, and S. Peacocka, "THE INFLUENCE OF PARTICLE SIZE ON RESPIRATORY INFECTION WITH ANTHRAX SPORES," *Journal of Hygiene* vol. 51, pp. 359-371, 1953.

[7] C. P. Wies, "Secondary Aerosolization of Viable Bacillus anthracis Spores in a Contaminated US Senate Office," *Journal of the American Medical Association,* vol. 288, pp. 2853-2858.

[8] N. P. Gao and J. L. Niu, "Modeling particle dispersion and deposition in indoor environments," *Aerosol Science,* vol. 41, pp. 3862-3876, 3 January 2007 2007.

[9] T. JS, "Turbulent entrainment: the development of the entrainment assumption, and its application to geophysical flows," *Journal of Fluid Mechanics,* vol. 173, pp. 431-471, 1986.

[10] B. CUSHMAN-ROISIN, *ENVIRONMENTAL FLUID MECHANICS*. New York: John Wiley and Sons, Inc., 2010.

[11] I. Wygnanski and H. Fielder, "Some measurements in the self-preserving jet. ," *J. Fluid Mech* vol. 38, pp. 577-612, 1969.

[12] S. Chhabra, T. N. Shipman, and a. A. K. Prasad, "The entrainment behavior of a turbulent axisymmetric jet in a viscous host fluid," *Exp. Fluid,* vol. 38, pp. 70-79, 2005.

[13] FLUENT, vol. 6.3.12.

[14] Q. Chen, "COMPARISON OF DIFFERENT K-E MODELS FOR INDOOR AIR FLOW COMPUTATIONS," *Numerical Heat Transfer Part B Fundamentals An International Journal of Computation and Methodology,* vol. 28.3, pp. 353-369, 1995.

[15] A. C. K. Lai and F. Z. Chen, "Comparison of a new Eulerian model with a modified Lagrangian approach for particle distribution and deposition indoors," *Atmospheric Environment,* vol. 41, pp. 5249-5256, 2007.

[16] C. T. Crowe, J. D. Schwarzkopf, M. Sommerfeld, and Y. Tsuji, *Multiphase Flows with Droplets and Particles*, 2nd ed.: CRC Press, 2011.

[17] S. HOLMBERG and Y. LI, "Modelling of the Indoor Environment – Particle Dispersion and Deposition," *Indoor Air,* vol. 8, pp. 113-122, 1998.

[18] L.-P. Wang and D. E. Stock, "Dispersion of Heavy Particles by Turbulent Motion," *Journal of Atmospheric Sciences,* vol. 50, pp. 1897-1913, 1993.

[19] M. Wang, C.-H. Lin, and Q. Chen, "Advanced turbulence models for predicting particle transport in enclosed environments," *Building and Environment,* pp. 40-49, 2011.

[20] Z. Zhang and Q. Chen, "Comparison of the Eulerian and Lagrangian methods for predicting particle transport in enclosed spaces," *Atmospheric Environment,* vol. 41, pp. 5236-5248, 2007.

[21] M. C. Roco, *Particulate Two-Phase Flow*: Butterworth-Heinemann 1993.

[22] W. C. Hinds, *Aerosol Technology: Properties, Behavior, and Measurment of Airborne Particles*. New York: John Wiley and Sons, Inc., 1999.

[23] P. G. Saffman, "The lift on a small sphere in a slow shear flow," *Journal of Fluid Mechanics,* vol. 32, p. 624, 1968.

[24] S. I. Rubinow and J. B. Keller, "The transverse force on a spinning sphere moving in a viscous fluid," *Journal of Fluid Mechanics,* vol. 11, pp. 447-459, 1961.
[25] A. T. HJELMFELT and L. F. MOCKROS, "MOTION OF DISCRETE PARTICLES IN A TURBULENT FLUID," *Applied Scientific Research,* vol. 16, pp. 149-161, 1965.
[26] R. Mei, R. J. Adrian, and T. J. Hanratty, "Particle Dispersion in isotropic turbulence under Stokes drag and Basset force with gravitational settling," *Journal of Fluid Mechanics,* vol. 225, pp. 481-495, 1991.
[27] H. M. Taylor and S. Karlin, *An Introduction to Stochastic Modeling,* 3rd ed. Chestnut Hill, MA: Academic Press, 1998.
[28] A. Li and G. Ahmadi, "Dispersion and Deposition of Spherical Particles from Point Sources in a Turbulent Channel Flow," *Aerosol Science and Technology,* vol. 16, pp. 209-226, 1992.
[29] K. S. Hayden, K. Park, and J. S. Curtis, "Effect of particle characteristics on particle pickup velocity," *Powder Technology* vol. 131, pp. 7-14, March 3 2003.
[30] D. Dasani, C. Cyrus, K. Scanlon, R. Du, K. Rupp, and K. H. Henthorn, "Effect of particle and fluid properties on the pickup velocity of fine particles," *Powder Technology,* vol. 196, pp. 237-240, 2009.
[31] E. Rabinovich and H. Kalman, "Pickup, critical and wind threshold velocities of particles," *Powder Technology,* vol. 176, pp. 9-17, July 10 2007.
[32] C. C.T., R. A. Gore, and T. R. Troutt, "Particle Dispersion by Coherent Structures in Free Shear Flows," *Particle Science and Technology,* vol. 3, p. 149, 1985.
[33] N. Kamula, F. Wen, T. R. Troutt, and C. T. Crowe, "Particle Dispersion by Ordered Motion in Turbulent Mixing Layers," *ASME Cavitation and Multiphase Forum,* vol. 64, 1988.
[34] F. Wen, "A Study on Particle Dispersion in a Two-Dimensional Mixing Layer " PhD Dissertation, Department of Mech. Engr. and Matls. Engr., Washington State University, 1990.
[35] G. WK, *Lectures in turbulence for the 21st century.* Göteborg, Sweden Department of Thermo and Fluid Engineering, Chalmers University of Technology, 2005.
[36] C. Casciola, P. Gualtieri, F. Picano, G. Sardina, and G. Troiani, "Dynamics of inertial particles in free jets," presented at the 2nd International Conference and Advanced School on Turbulent Mixing and Beyond, 2010.
[37] D. F. Tatterson, T. L. Marker, and J. M. Forgac, "Particle effects on free jet entrainment. ," *The Canadian Journal of Chemical Engineering,* vol. 65, pp. 361-365, 1987.
[38] J. R. Ferguson and D. E. Stock, ""Heavy" Particle Dispersion Measurements with Mono- and Polydisperse Particle Size Distributions," in *Winter Annual Meeting of the American Society of Mechanical Engineers,* Atlanta, GA, 1991, pp. 53-58.
[39] S. Elghobashi, "On predicting particle-laden turbulent flows," *Applied Scientific Research* vol. 52.4, pp. 309-329, 1994.
[40] R. A. Gore and C. T. Crowe, "Modulation of turbulence in a dispersed phase," *ASME Journal of Fluid Engineering,* vol. 114, pp. 304-307, 1991.
[41] G. Hetsroni, "Particle-turbulence interaction," *International Journal of Multiphase Flow,* vol. 15, pp. 735-746, 1989.
[42] J. DeSpirito and L.-P. Wang, "Linear instability of two-way coupled particle-laden jet," *International Journal of Multiphase Flow,* vol. 27, pp. 1179-1198, July 2001 2001.
[43] X. L. Tong and L. P. Wang, "Two Way Coupled Particle-Laden Mixing Layer Part 1: Linear Instability " *International Journal of Multiphase Flow,* vol. 25, pp. 575-598, 1999.

Appendix A: Comparison of Initial Simulations to Experimental Results

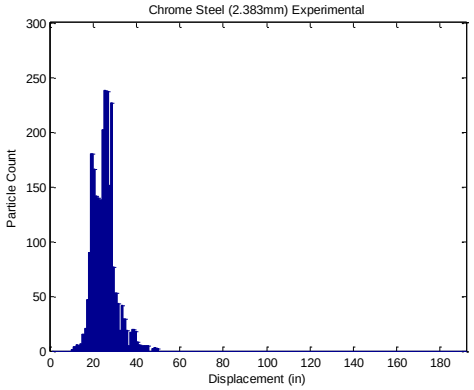

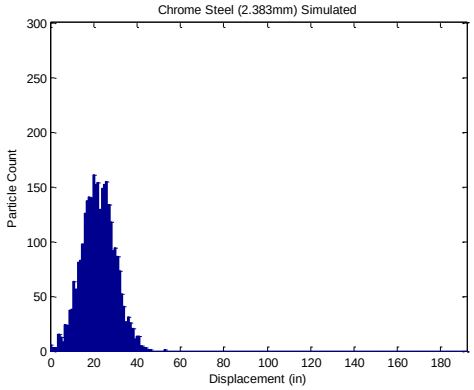

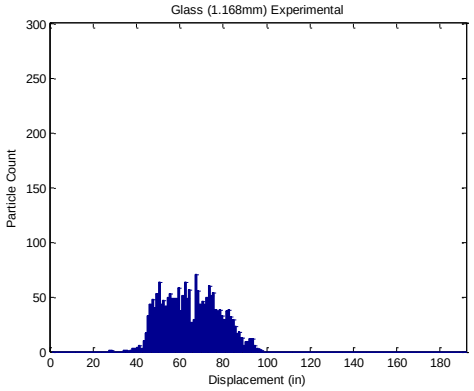

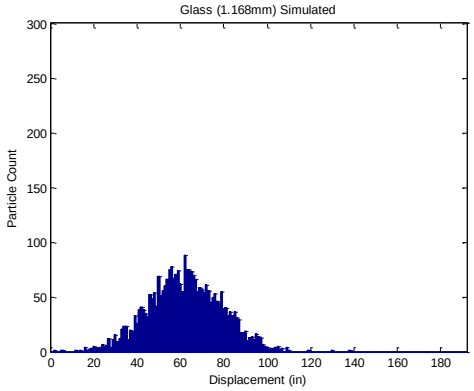

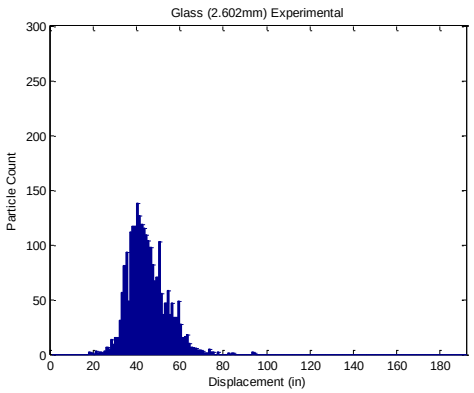

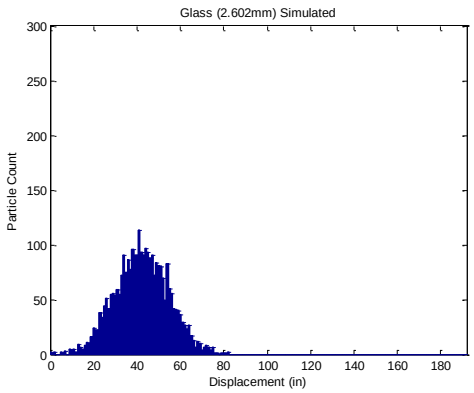

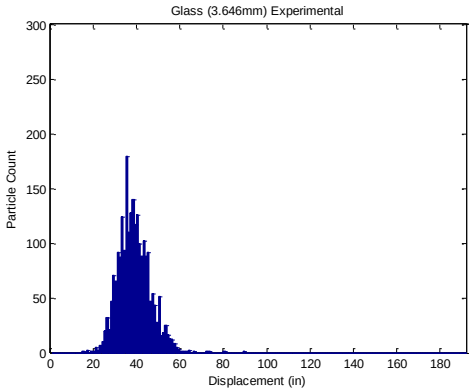
Glass (3.646mm) Experimental
Particle Count
Displacement (in)

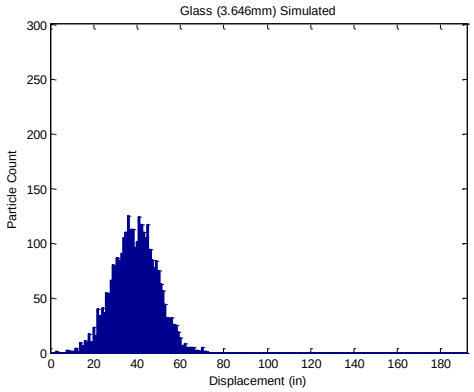
Glass (3.646mm) Simulated
Particle Count
Displacement (in)

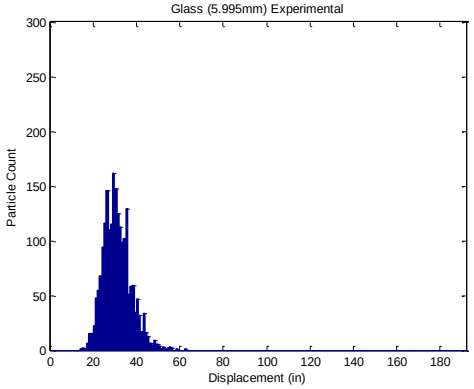
Glass (5.995mm) Experimental
Particle Count
Displacement (in)

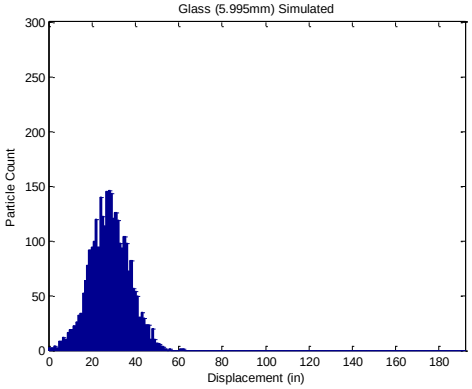
Glass (5.995mm) Simulated
Particle Count
Displacement (in)

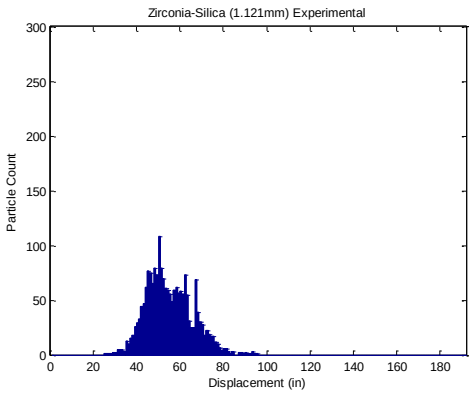
Zirconia-Silica (1.121mm) Experimental
Particle Count
Displacement (in)

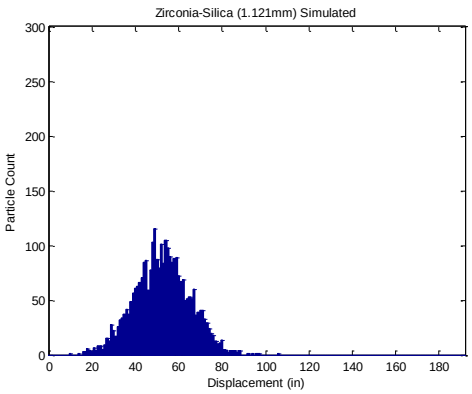
Zirconia-Silica (1.121mm) Simulated
Particle Count
Displacement (in)

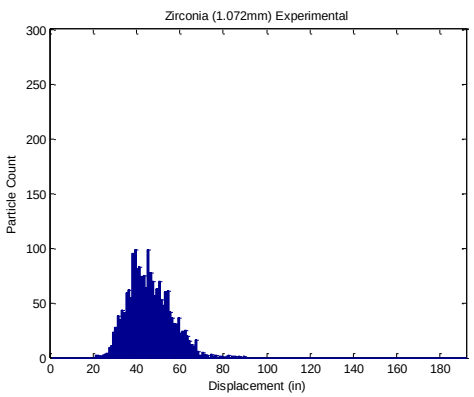
Zirconia (1.072mm) Experimental
Particle Count
Displacement (in)

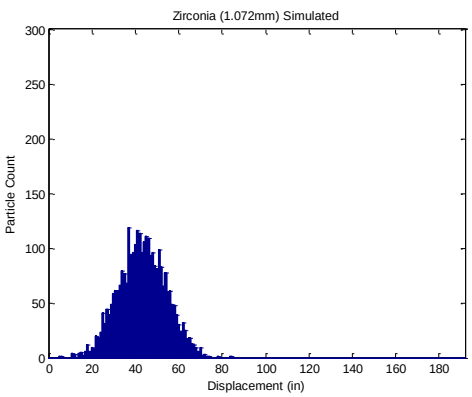
Zirconia (1.072mm) Simulated
Particle Count
Displacement (in)